
Article:
Xie, P. orcid.org/0000-0001-7156-7061, Lu, X., Ding, H. et al. (4 more authors) (2019) A mesoscale 3D CFD analysis of the liquid flow in a rotating packed bed. Chemical Engineering Science, 199. pp. 528-545. ISSN 0009-2509

https://doi.org/10.1016/j.ces.2019.01.038

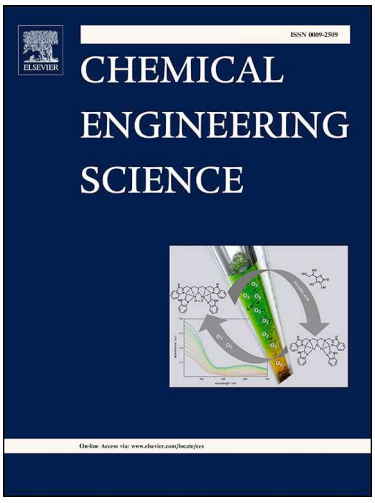

A mesoscale 3D CFD analysis of the liquid flow in a rotating packed bed

Peng Xie, Xuesong Lu, Hongbing Ding, Xin Yang, Derek Ingham, Lin Ma, Mohamed Pourkashanian

PII: S0009-2509(19)30120-4
DOI: https://doi.org/10.1016/j.ces.2019.01.038
Reference: CES 14752

To appear in: *Chemical Engineering Science*

Received Date: 4 December 2018
Revised Date: 26 January 2019
Accepted Date: 30 January 2019

Please cite this article as: P. Xie, X. Lu, H. Ding, X. Yang, D. Ingham, L. Ma, M. Pourkashanian, A mesoscale 3D CFD analysis of the liquid flow in a rotating packed bed, *Chemical Engineering Science* (2019), doi: https://doi.org/10.1016/j.ces.2019.01.038

A mesoscale 3D CFD analysis of the liquid flow in a rotating packed bed

Peng Xie[a], Xuesong Lu[a], Hongbing Ding[a,b], Xin Yang[a], Derek Ingham[a], Lin Ma[a,*], Mohamed Pourkashanian[a]

[a]Energy 2050, Department of Mechanical Engineering, Faculty of Engineering, University of Sheffield, Sheffield S10 2TN, UK

[b]Tianjin Key Laboratory of Process Measurement and Control, School of Electrical and Information Engineering, Tianjin University, Tianjin 300072, China

[*]Corresponding author:

Email: lin.ma@sheffield.ac.uk Phone: +44 (0) 114 21 57212

Abstract

Rotating packed beds (RPBs), as a type of process intensification technology, are promising to be employed as high-efficiency CO_2 absorbers. However, the detailed understanding of the liquid flow in the RPB is still very limited. The complex and dense packing of the bed and the multiscale of the RPB make it very difficult to perform numerical simulations in detail, in particular for full 3D simulations. In this paper, a mesoscale 3D CFD modelling approach is proposed which can be used to investigate the liquid flow in both laboratory- and large-scale RPBs in detail and accuracy. A 3D representative elementary unit of the RPB has been built and validated with experimental observations, and then it is employed to investigate the gas–liquid flows at different locations, across a typical RPB, so that the overall characteristics of the liquid flow in the RPB can be assembled. The proposed approach enables the detailed prediction of the liquid holdup, droplets formation, effective interfacial area, wetted packing area and specific surface area of the liquid within real 3D packing structures throughout the bed. New correlations to predict the liquid holdup, effective interfacial area, and specific surface area of the liquid are proposed, and the sensitivities of these quantities to the rotational speed, liquid flow rate, viscosity and contact angle have been investigated. The results have been compared with experimental data, previous correlations and theoretical values and it shows that the new correlations have a good accuracy in predicting these critical quantities. Further, recommendations for scale-up and operation of an RPB for CO_2 capture are provided. This

proposed model leads to a much better understanding of the liquid flow behaviours and can assist in the RPB optimisation design and scaling up.

Keywords: rotating packed bed, CFD, liquid holdup, interfacial area, flow pattern, VOF model

1. Introduction

1.1. Introduction of the RPB and its investigation

Rotating packed beds (RPBs), which utilize a rotating porous component to generate a high centrifugal field, are very important means of process intensification (PI). A schematic diagram of a typical RPB is shown in Fig. 1. Packing is a central component of the RPB, typically made of wire meshes or metal sheets forming complex 3D pore structures. In the operation of the RPB, a solvent is radially injected into the packing region from the liquid distributor located at the centre of the bed, and gas can be fed into the bed from the periphery, or the centre of the bed to form a counter-current or co-current gas-liquid configuration, respectively. The rotating porous packing turns the continuous liquid into thin films and tiny droplets through the action of the shear, which significantly increases the interfacial area and consequently promotes the mass transfer between the liquid phase and the gas phase that flows through the RPB (Yan et al., 2014). In addition, there are other advantages of the RPB, such as the small footprint, the short-time response to meet the control requirements, the ability to deal with fluids with high viscosity (Wang et al., 2015). Due to these prominent advantages, it has been successfully applied in the separation process (Chen and Liu, 2002; Chu et al., 2014; Zou et al., 2017), reaction process (Chen et al., 2010), engineering of nanoparticles (Chen et al., 2000), etc. since it was first proposed by Ramshaw and Mallinson (1981).

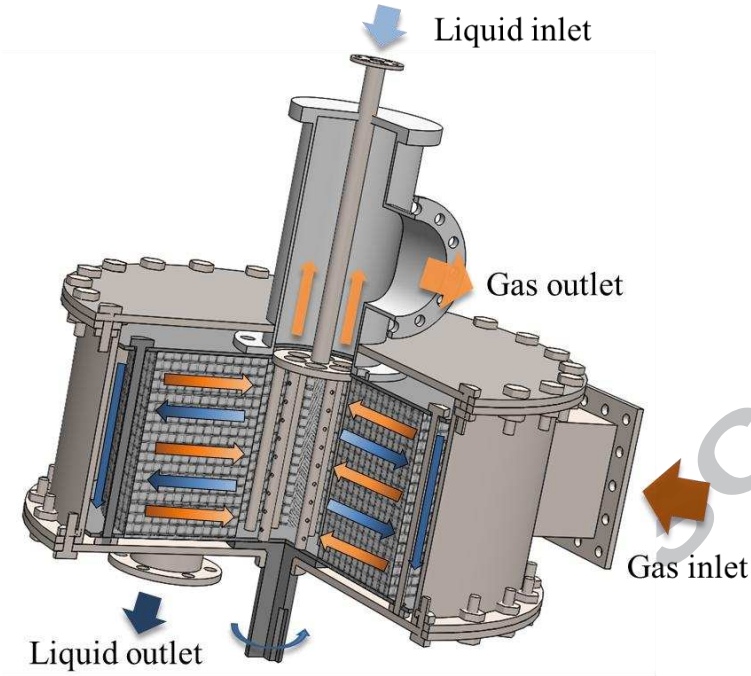

Fig. 1. Schematic diagram of a typical RPB with a counter-current flow configuration.

In recent years, in the context of global carbon emission mitigation, there is a great demand for high-efficient and low-cost CO_2 capture technology. The solvent-based post-combustion CO_2 capture (PCC) by chemical absorption using amines, which is suitable for retrofitting to the existing power plants and being incorporated into the new power plants, is one of the promising CO_2 capture technologies for commercial deployment. However, the rate of CO_2 capture by amines, through the conventional separation technology (i.e. packed columns), is limited by the relatively slow mass transfer process (Biliyok et al., 2012). Therefore, the RPB has the potential to replace the packed columns in the PCC process to achieve a higher mass transfer efficiency, less equipment footprint, less equipment investment, and it can deal with high-concentrated amine-based solvents more efficiently (Jassim et al., 2007; Wang et al., 2015; Yu et al., 2016; Zhao et al., 2014).

The detailed understanding of the liquid flow behaviours, which determines the mass transfer performance, is significant for the optimum design and scale-up of the RPB. At present, different measuring techniques have been used to measure the fluid dynamics in RPBs. These include (i) non-invasive measuring techniques, such as the high-speed photography (Burns and Ramshaw, 1996; Guo et al., 2000; Sang et al., 2017), particle image velocimetry (PIV) (Yang et al., 2011), X-ray computed tomography (Yang et al., 2015a), and (ii) invasive measuring techniques, such as tracking the liquid trajectories in the RPB by inserting papers (Yan et al., 2012) or wrapping paper tapes (Guo et al., 2014).

Although these experimental methods assist us in forming some understanding of the liquid behaviour within RPBs, there are still some great challenges for accurately describing the liquid flow in the RPB. In particular: (i) It is very difficult to directly measure the gas/liquid and liquid/packing interfacial areas in the RPB with different gas/liquid/packing systems, which impedes the accurately prediction of the mass transfer and drag force between them. (ii) There is no feasible method to obtain the volume ratio of the droplets to the liquid films at present, thus the flow model has not been fully described.

1.2. CFD modelling of the RPB

Compared with the experiments, CFD simulations have unique advantages, for example, they can visually present the detailed liquid hydrodynamic and mass transfer behaviour in the complex inner space of the chemical equipment, which is often difficult to obtain through experimental measurements (Lopes and Quinta-Ferreira, 2009; Yang et al., 2016). At present, CFD simulations of the RPB have been performed based on both the single and two-phase models (Yang et al., 2018). For the single-phase simulation, the porous media model based on empirical formulae have mostly been used to describe the resistance of the packing to the gas phase (Llerena-Chavez and Larachi, 2009; Wu et al., 2018; Yang et al., 2015b). This is in order to avoid directly resolving the flow field in the actual geometry of the packing, which requires a large number of computational grids and consequently a large amount of computational resource (Liu et al., 2017). For the two-phase flow modelling, the volume of fluid (VOF) model is mostly employed since it can calculate the interface between the gas and liquid, and significant progress has been achieved in predicting the overall behaviour of the liquid flow in the RPB. For example, gas-liquid flow (Shi et al., 2013), mass transfer (Yang et al., 2016), micromixing (Guo et al., 2016) and end effect (Ouyang et al., 2018) in the RPBs were simulated in 2D calculation domains, where the wire mesh packings are simplified as small square blocks. Xie et al. (Xie et al., 2017b) investigated the liquid holdup and liquid dispersion in the RPB through employing a 2D calculation with small circle blocks closely representing the actual wire mesh packings. In addition, Guo et al. (Guo et al., 2017) simulated the liquid flow in an RPB through employing a 3D VOF model, where the wire mesh packing is simplified as small cylinders. Compared to the 2D VOF model, the 3D VOF model is more accurate in simulating the liquid flow in the RPB; however, due to the extremely complexed structure and small scales of the pores in the RPB, it requires an extremely large number of computational grids to resolve the pore structure. Although the VOF method theoretically allows the resolution of the detailed geometry of the RPB, it is very difficult to meet

the requirement of performing transient calculations for the full 3D simulation of even a laboratory-scale RPB with appropriate accuracy (Guo et al., 2017).

In order to improve the understanding of the real gas/liquid flow in the pores of the packing, detailed and more accurate 3D simulations of the flow in the real geometrical structure of the packing are necessary. However, due to the multiscale issues that have plagued the modelling of the RPB, the multiscale modelling strategy has to be taken into account and the mesoscale 3D modelling of the flow over the packing structure/pores is the most important aspect of the analysis. At present, simulating the pressure drop (Llerena-Chavez and Larachi, 2009; Lu et al., 2018; Wu et al., 2018; Yang et al., 2015b) and liquid holdup (Lu et al., 2018) in the RPB by using a porous media model can be considered as the macroscale CFD modelling. This method does not resolve the geometrical structure of the packing in the RPB, and therefore it can be used to simulate large-scale RPBs without using too much computing resources. However, currently there is substantial difficulty in finding a generally applicable model that accurately describes the drag force between the gas and liquid, the gas and solids and the liquid and solids in the RPBs. On the other hand, some CFD models have focussed on the details of the gas-liquid flow and mass transfer on the gas-liquid interface of thin liquid films (Albert et al., 2014; Hu et al., 2014; Xie et al., 2017a) and single droplets (Bothe and Fleckenstein, 2013; Ozkan et al., 2016), and these can be regarded as the microscale CFD simulations. Mesoscale CFD studies of a packed bed refer to the CFD simulations of the flow at a scale that is comparable to the dimensions of a typical packing unit (Li et al., 2016; Liu et al., 2016; Raynal and Royon-Lebeaud, 2007; Sebastia-Saez et al., 2015a; Singh et al., 2018; Sun et al., 2013). The characteristics of the liquid flow in the mesoscale affect both the performance of the microscale mass transfer and overall performance of the RPB, such as the overall pressure drop and liquid flooding.

Therefore, in this paper, a mesoscale CFD model is proposed to investigate the liquid flow in the RPB. The mesoscale model is based on a small 3D representative elementary unit (REU), being implemented at different locations in an RPB. Through this model, the influence of the operating conditions and the properties of the packings and liquids on the local hydrodynamic characteristics are investigated. In addition, new correlations for predicting the distribution of the liquid characteristic parameters in the whole RPB are developed based on the local data.

2. CFD model

2.1. Representative elementary unit (REU) of the RPB

Fig. 2(a) shows a cross section of the packing area of a pilot-scale RPB, with a bed of 0.1 m inner radius, 0.5 m outer radius and 0.2 m thickness, which is investigated in this paper. The RPB is operated at 100-300 rpm and the liquid flow rate ranges from 7.2-21.6 m^3/h. In the RPB, the liquid is radially injected into the packing from the centre of the RPB through a liquid distributor. Due to the structure of the packing being repeated in the circumferential and axial directions of the RPB and the flow is dominated by the packing, the idea of representative elementary unit (REU) is proposed in order to reduce the computational cost, which has been used in both the single-phase system (Qi et al., 2017) and the multiphase system (Sebastia-Saez et al., 2015a; Singh et al., 2018). As demonstrated in Fig. 2(a), a small REU can be identified (Fig. 2(b) and (c)) at locations of interest in the RPB. Then the local liquid flow at these positions can be simulated with appropriate boundary conditions, such as the liquid flow rate and centrifugal acceleration, to the REU. The VOF model is used to capture the gas-liquid interface in the REU and the centrifugal force field in the REU is simulated using a rotating reference frame.

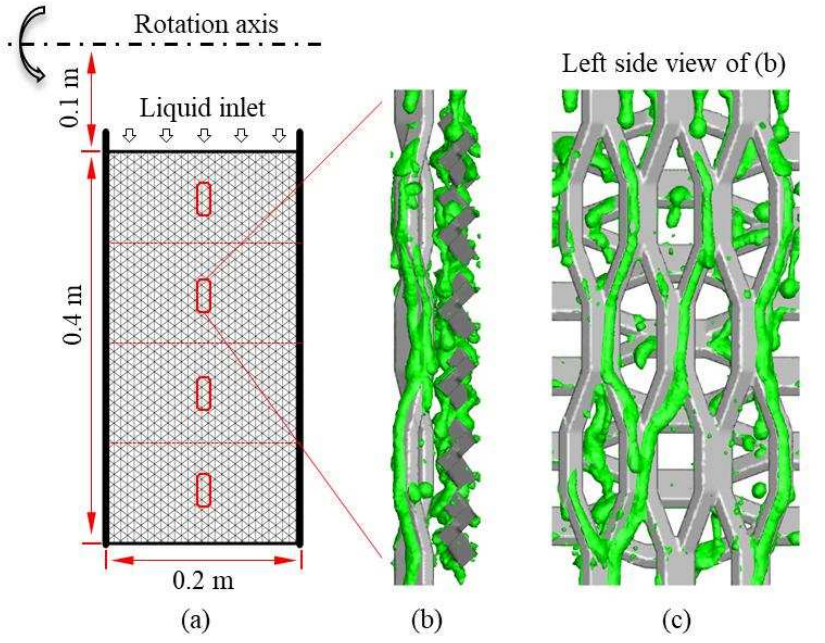

Fig. 2. (a) Schematic diagram of the bed of the simulated RPB, (b) schematic diagram of the REU and (c) left side view of (b).

From the existing studies (Guo et al., 2000; Ouyang et al., 2018; Xie et al., 2017b; Yan et al., 2012), there are two regions, i.e. the entrance region and the bulk region, in the packed bed of the RPB. In the entrance region, the liquid interacts with the rotating packing, and obtains the tangential velocity of the packing. Almost all the liquid can be captured by the packing within approximately 10 mm from the entrance (Guo et al., 2000) and then the liquid closely follows the rotation of the bed. In a pilot-scale or industrial-scale RPB with a large diameter, the size of the entrance region in terms of the percentage of the bed size becomes very small. For example, if the depth of the entrance region is assumed to be 10 mm in the RPB, as investigated in this paper, it only takes 2.5% of the total depth of the bed. Therefore, the focus of this investigation is the bulk region, and the liquid can be assumed to be evenly distributed in the circumferential direction according to the experimental observations (Yan et al., 2012) and simulations (Ouyang et al., 2018). As a future work, a submodel for the entrance region may be developed in order to take into account in more detail the end-effect of the RPB.

In addition, special attention should be paid to the packing due to its strong effect on the gas-liquid hydrodynamics and mass transfer performance. Stainless steel meshes are widely employed as the packings of RPBs due to their high mass transfer performance (Chen et al., 2006) and their resistance to corrosion. At present, most of the stainless steel meshes used in the RPBs are knitted or woven stainless steel wire mesh. However, these meshes have poor repeatability in construction as well as low mechanical strength (Luo et al., 2017). Therefore, the expanded stainless steel mesh packing, which has been used for investigating CO_2 absorption by monoethanolamine (MEA) solutions (Jassim, 2002), is employed in this study, as shown in Fig. 3(a). The mesh is manufactured through expanding the stainless steel sheet, and this enhances the material strength during the expansion, hence it has sound reliability for the industrial RPBs for long-time operation. In addition, there is almost no waste material from the manufacturing process and this is because the base metal is cut and stretched to the final form (Smith et al., 2009). Typically, the expanded stainless steel mesh sheets are cut into annular shapes and they are stacked along the axial direction of the rotor layer by layer to form a firm packed bed. In order to increase the porosity of the packing, and make the liquid evenly distributed, the mesh is configured to be 90° between the two adjacent sheets. Therefore, every two packing layers form a repeating structure in the axial direction of the bed and the fluid flows between the two sheets from the top to the bottom (see Fig. 2(b) and (c)). In addition, along the radial direction from the inner periphery to the outer periphery, the packing also can be

regarded as being made up of many duplicate structures. The structure of the minimum unit of the expanded metal mesh is shown in Fig. 3(b) and the structural dimensions of the packing are listed in Table 1. Based on this configuration, the specific surface area of the packing is 546.5 m^2/m^3 and the void fraction is 0.84.

The size of the REU is determined through considering both the periodicity of the packing and the mesh numbers. The dimensions of the REU in the circumferential and axial directions are the minimum periodic distance of the packing, which are 15.81 mm and 5.7 mm respectively. While, due to a certain distance being required for the development of the liquid along the radial direction, the distance of the two minimum periodic units (31.62 mm) are taken as the dimension of the REU in the radial direction after investigating the effect of the liquid inlet configuration on the liquid distribution (this is discussed in Section 3.3).

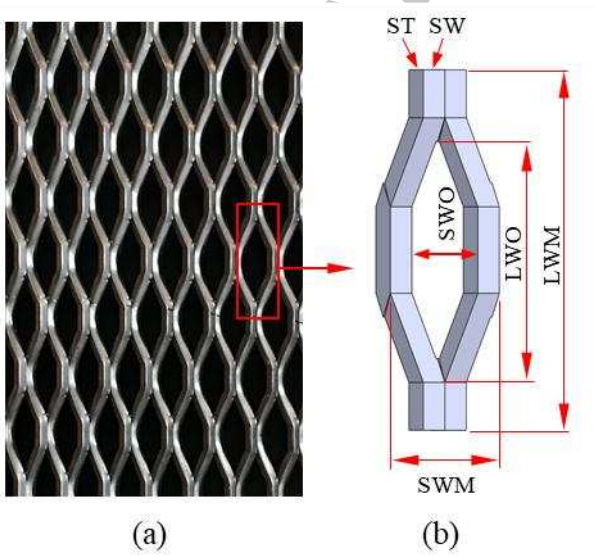

Fig. 3. (a) Photograph of the expanded stainless steel mesh and (b) a schematic of the minimum unit.

Table 1. Structural dimensions of the expanded stainless steel mesh packing.

Name	Dimensions (mm)
Long way of the mesh (LWM)	15.81
Short way of the mesh (SWM)	4.78
Long way of the opening (LWO)	10.57
Short way of the opening (SWO)	2.90
Strand width (SW)	1.33

Strand thickness (ST)	0.90

2.2. Computational grid and boundary conditions of the REU

In order to prevent numerical difficulties associated with the quality of the grid generated, some special treatments have been adopted in the model. For example, chamfering has been performed to avoid the sharp corners at the splits. In addition, there is a 0.2 mm gap in the nearest location between the packing sheets rather than them touching each other through contact points, and this value is chosen based on trial and error. These treatments have been employed in the literature (Lopes and Quinta-Ferreira, 2009; Nijemeisland and Dixon, 2001). Then the calculation domain is discretized with an unstructured mesh as shown in Fig. 4. Prism grids with a higher grid density is implemented near the packing surface in order to capture the thin liquid film accurately, and in other regions, the grid is tetrahedral mesh dominate. The final grid size is a result of a grid sensitivity study, which is discussed in more detail in Section 3.1. In this paper, the geometry is generated using SOLIDWORKS 2015, and the computational gird is generated using ICEM CFD 17.2.

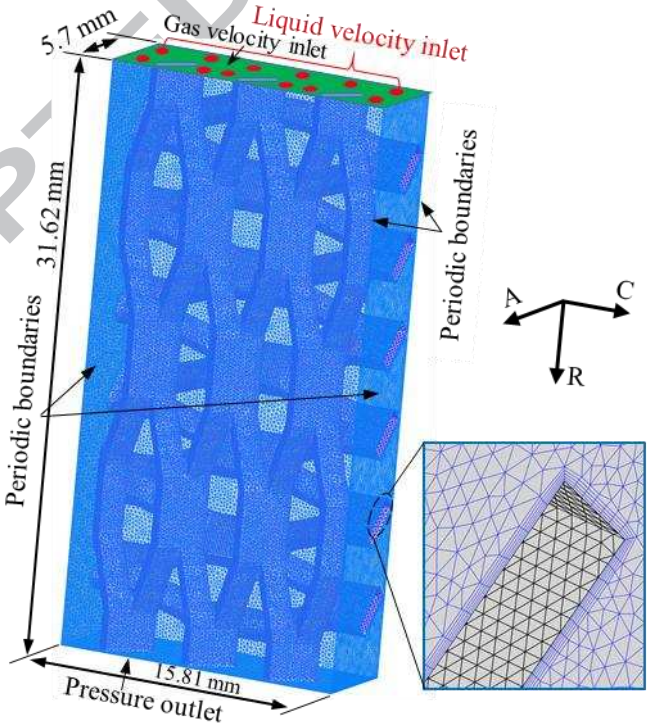

Fig. 4. Computational domain, boundary conditions and grids for the REU (A stands for the axial direction, C stands for the circumferential direction and R stands for the radial direction in the RPB).

The liquid superficial velocity (U), namely the liquid flow rate per unit annular cross-section area of the RPB, is calculated according to the following equation:

$$U = \frac{Q_L}{2\pi r h} \quad (1)$$

where Q_L is the volume flow rate of the liquid, r is the radial position of the REU in an RPB, h is the thickness of the packed bed in the axial direction of an RPB.

Therefore, for a given operating condition, the volume flow rate of the liquid feeding the REU is calculated as follows:

$$q_L = U \cdot A \quad (2)$$

where A is the entrance area of the REU, see Fig. 4. Due to the short distance of the calculation domain in the radial direction compared to the radius of a pilot-scale RPB, the cross section area along the radial direction in the REU is assumed constant and equal to A.

According to the visualization study (Burns and Ramshaw, 1996), the flow pattern in the RPB could be a combination of droplet, film and pore flows at different conditions. Therefore, it is very difficult to pre-set the liquid inlet boundary conditions to be the same as the actual flow patterns. Fortunately, investigations (Ding et al., 2018; Xu et al., 2014b) indicate that the liquid after flowing around an object will develop into different flow patterns within a short distance that mainly depends on the liquid flow rate, the surface properties of the object, etc. rather than the liquid inlet condition. Therefore, in this paper, the liquid is set such that is fed from several evenly distributed nozzles. After the liquid flows out of the nozzles, it interacts with the packings and then quickly develops into different flow patterns at different conditions. In addition, a distance is required to make the liquid flow develop into a pseudo steady state, and the effect of the liquid inlet configuration on the liquid distribution along the radial direction in the REU is discussed in Section 3.3.

Many investigations indicate that the gas has little effect on the liquid flow below the flooding point (Chen et al., 2004; Guo et al., 2000; Lin et al., 2000), and this is mainly because the density of the gas is much lower than that of the liquid. In addition, due to the VOF model using a set of momentum equations for the gas-liquid two-phase flow, and it is not recommended to simulate the conditions for which the gas and liquid have a very large velocity difference. Therefore, the gas and liquid is set at a co-current configuration in the simulation, and the effects of the gas flow on the liquid flow characteristics are not precisely investigated in this paper. The setting of the inlet boundary conditions of the REU is

implemented through the user-defined functions (UDFs), where the liquid volume fraction is specified as unity in the liquid nozzle region, and zero in the rest of the inlet region, which is the gas inlet region (see Fig. 4). At the inlet, the gas and liquid are assumed to have the same circumferential velocity with the packing. The radial liquid inlet velocity is calculated based on the following equation:

$$u_0 = \frac{q_L}{A_N} \tag{3}$$

where A_N is the total area of the liquid nozzles in the REU. The radial velocity of the gas is set as 20% of the radial liquid velocity in the gas inlet area to reduce the backflow from the outlet and accelerate convergence.

For the surface of the packing, the no-slip boundary condition and the wall adhesion are specified. However, a given packing material may have different contact angles depending on the surface treatment technologies and the liquid properties, and for a given liquid, the contact angle also varies with different packing surfaces (Sebastia-Saez et al., 2018; Singh et al., 2016, 2018; Zhang et al., 2017). In addition, the contact angle of the expanded stainless steel packing surface corresponding to different solvents is not available in the literature. Therefore, a value of 75° is specified as the contact angle of the packing surface in the initial simulations since this is within the reasonable range for stainless steel (Sebastia-Saez et al., 2018) and it is suitable for the packings used in RPBs (Zhang et al., 2017). Further, in order to investigate the effect of the contact angle on the flow pattern, liquid holdup and interfacial area, the contact angle ranging from 30° to 120° is studied in this paper. Due to the thickness of the REU being much smaller than the thickness of the bed in the axial direction, most of the liquid flow in the RPB is not effected by the sidewalls of the RPB, and the liquid flow is mainly dominated by the periodic packing structure. Therefore, the periodic boundaries are used for axial simplification. In addition, due to the REU being assumed to be repeatable in the circumferential directions of the RPB, the left and right surfaces of the REU as shown in Fig. 4 are set to be periodic boundaries as well. The outlet boundary is set as the pressure outlet and the pressure is equal to one standard atmospheric pressure.

Aqueous MEA solutions are the typical absorbents employed for CO_2 capture, and 30 wt% MEA aqueous solution is normally used in the packed columns for CO_2 capture. The RPB has the advantage to deal with a highly concentrated MEA solution than packed columns because of the strong centrifugal field that can break the liquid and significantly increase the specific surface area of the solvent (Chen et al., 2005). Therefore, simulations are performed with a variety of aqueous MEA solutions with the

concentration from 30 wt% to 90 wt%. In addition, for the model validation, water and glycerol solution are also adopted. The properties of the solvents used for the CFD simulations are listed in Table 2. The MEA is assumed to operate at a constant temperature of 40 ^{o}C, which is close to the real operation conditions of a CO_2 absorber employed for PCC.

Table 2. Physical properties of the solvents used for the CFD simulations. [a]

Solvent	Density/(kg/m^3)	Kinetic viscosity/(mm^2/s)	Surface tension/(N/m)
Water	998.2	1.00	0.07280
30 wt% MEA (Amundsen et al., 2009)	1003.4	1.66	0.05352
50 wt% MEA (Amundsen et al., 2009)	1011.7	3.35	0.05069
70 wt% MEA (Amundsen et al., 2009)	1015.5	6.85	0.04888
90 wt% MEA (Amundsen et al., 2009)	1008.4	10.12	0.04725
70 wt% glycerol (Yang et al., 2015a)	1173.0	15.77	0.06650

[a] The properties of the aqueous MEA solutions are at 40 ℃.

2.3. Governing equations

Gas and liquid in the REU are assumed to be incompressible fluids, and the VOF model, originally proposed by Hirt and Nichols (1981), is adopted to track the gas-liquid interface in this paper. This because it has been widely used in the CFD modelling of the detailed multiphase flow in the 3D packings of various packed beds (Guo et al., 2017; Li et al., 2016; Singh et al., 2017; Sun et al., 2013; Xu et al., 2014a). In the VOF model, a single set of momentum equations are shared by the two fluids, and the volume fraction of each of the fluids in each computational cell is tracked throughout the domain. In order to simulate the flow in the REU of the RPB, a rotational moving reference frame is employed (Xie et al., 2017b). The governing equations of the fluid flows in the moving reference frame may be written as follows:

The continuity equation and the volume fraction equation:

$$\frac{\partial}{\partial t}(\alpha_l \rho_l) + \nabla \cdot (\alpha_l \rho_l \vec{v}_{lr}) = 0 \tag{4}$$

$$\alpha_g = 1 - \alpha_l \tag{5}$$

The momentum conservation equation:

$$\frac{\partial}{\partial t}(\rho \vec{v}_r) + \nabla \cdot (\rho \vec{v}_r \vec{v}_r) + \rho(2\vec{\omega} \times \vec{v}_r + \vec{\omega} \times \vec{\omega} \times \vec{r}) = -\nabla p + \nabla \cdot \left[\mu\left(\nabla \vec{v}_r + \nabla \vec{v}_r{}^T\right)\right] + \vec{F}_{vol} \tag{6}$$

where α_l, α_g is the volume fraction of the liquid phase and gas phase, respectively, and $\vec{v}_{lr}$ is the relative velocity for liquid phase; $(2\vec{\omega} \times \vec{v}_r)$ and $(\vec{\omega} \times \vec{\omega} \times \vec{r})$ are the Coriolis acceleration and the centripetal

acceleration at the location r with a rotational speed ω, respectively. When the value α_l of a computational cell is equal to zero, it indicates that the cell is full of the gas phase, and when α_l=1, this means the cell is full of liquid, and when 0<α_l<1, the cell contains the gas-liquid interface. The interface is reconstructed by the Geometric-Reconstruction scheme (Youngs, 1982), which uses a piecewise-linear approach to represent the interface between the fluids. The fluid properties, such as density ρ and dynamic viscosity μ, take volume-averaged values of the two phases in each cell.

The effect of the surface tension is introduced in this model through employing the CSF (Continuum Surface Force) model proposed by Brackbill et al. (1992), i.e. the surface tension force is transformed to a volume force source term F_{vol} in the momentum equations. The localised volume force F_{vol} is calculated using the following equation:

$$F_{vol} = \sigma \frac{\rho k \nabla \alpha_l}{0.5(\rho_l + \rho_g)} \tag{7}$$

where σ is the surface tension coefficient, and k is the gas-liquid interface curvature. In addition, the effect of the contact angle between the fluid and the wall is established within the framework of the CSF model by changing the unit surface normal at the grid next to the wall.

Flow in the packing region is complicated. As described by Yan et al. (2014), although the Reynolds number based on the size of the pore/wire is usually low, part of the laminar liquid film flow near the packing surfaces develops into turbulence flow; therefore, partially turbulent flow could exist in the packing region. The SST k-ω model that was presented by Menter (1994) incorporates modifications for low-Reynolds number effects and it presents a good ability for describing the detailed flow in the RPB (Xie et al., 2017b). In addition, the turbulence parameters in the calculation domain have been checked in the preliminary studies, and it was found that the turbulent viscosity ratio is less than 0.5 in most of the region, and the largest turbulent viscosity ratio is about 2.5, which means that the level of the turbulence is weak in the calculation domain. Therefore, the SST k-ω model is adopted in this paper. It is worth mentioning that the turbulence modelling in packed materials is currently still a topic of much ongoing research.

2.4. Numerical scheme

Simulations are performed using the ANSYS Fluent 17.2 software that incorporates the in-house developed UDFs for setting the inlet boundaries. The pressure-velocity coupling is resolved by the

Pressure Implicit with Splitting of the Operators (PISO) algorithm and the Body Force Weighted scheme is employed for the pressure discretization. The gradient of the variables is calculated through using the least-squares cell based method, and the warped-face gradient correction is enabled to improve the gradient accuracy for the complex unstructured grids (ANSYS Inc, 2016). The Geo-Reconstruct scheme is applied for the spatial discretization of the volume fraction equation, the second-order upwind scheme is employed for solving the momentum equations and turbulence equations. Due to the presence of large body forces (including centrifugal forces and surface tension forces) in the calculation domain, the "implicit body force" is enabled for improving the solution convergence by accounting for the partial equilibrium of the pressure gradient and body forces in the momentum equations. In addition, in each calculation, the residuals in all the equations less than 1×10^{-4} are considered as the convergence criterion. Different time step sizes have been tested to check the effect of the time step size on the results. As a result, the time step size is set as 5×10^{-7} s when the centrifugal acceleration is no more than 100 m/s^2 and it is less than 3×10^{-7} s when the centrifugal acceleration is between 100 m/s^2 to 300 m/s^2. In addition, the maximum number of iterations of 20 are performed per time step in order to achieve the calculation convergence. The instantaneous liquid holdup, wetted wall area and gas-liquid interfacial area are monitored for each simulation to ensure it achieves the pseudo steady state, and the average value of the parameters in each simulation are calculated based on the instantaneous value after the simulation achieves the pseudo steady state. All the simulations are performed using the High Performance Computing (HPC) cluster in the University of Sheffield.

3. Model verification and validation

3.1. Grid convergence analysis

A verification study is undertaken to determine a reasonable computational grid size and to assess the error estimate (δ) and grid uncertainty (U_G). Three different grids consisting of 0.92, 1.40 and 2.48 million cells have been employed to investigate the effect of the grid size on the effective interfacial area A_e (defined in Section 4.2.1). The test liquid is 50 wt% MEA and the superficial velocity employed in the test is 0.0106 m/s. The verification is performed at two centrifugal conditions, with the centrifugal acceleration of 74.0 m/s^2 and 205.6 m/s^2, which are equivalent to the centrifugal accelerations at r=0.3 m with the bed rotational speed of N=150 rpm and 250 rpm, respectively. As shown in Fig. 5, A_e decreases with the increasing mesh numbers at the same centrifugal field, and this is mainly due to the false diffusion errors

near the gas-liquid interface decrease with the grid refinement. The U_G analysis is performed through using the Richardson extrapolation method with the recommended factors of safety (FS_0=2.45, FS_1=1.6, FS_2=6.9) (Xing and Stern, 2010, 2011). In the factor of safety (FS) method, the error estimate is $\delta=P*\delta_{RE}$, where P is the distance metric to the asymptotic range and δ_{RE} is the error estimate from the Richardson extrapolation method. The detailed calculation procedure can be found in the references (Xing and Stern, 2010, 2011) and the results of the grid convergence study are listed in Table 3. The convergence ratio R_K is between 0 and 1 both at g=74.0 m/s^2 and g=205.6 m/s^2, which means that monotonic convergence is achieved at the two typical test conditions. In addition, at the condition of 74.0 m/s^2, δ=0.96 and the relative U_G=3.42%. At the condition of 205.6 m/s^2, δ=7.92 and the relative U_G=26.07%. This indicates that at a higher centrifugal field, the dispersed liquid in the calculation domain becomes smaller, therefore, a fine grid is required in order to accurately capture the gas-liquid interface. However, a finer grid requires more computing memory and computing time. Both considering the computing efficiency and the simulation precision, the grid with 2.48M cells is used when the centrifugal acceleration is between 100 m/s^2 and 300 m/s^2, and the grid with 1.40M cells is used when the centrifugal acceleration is less than 100.0 m/s^2.

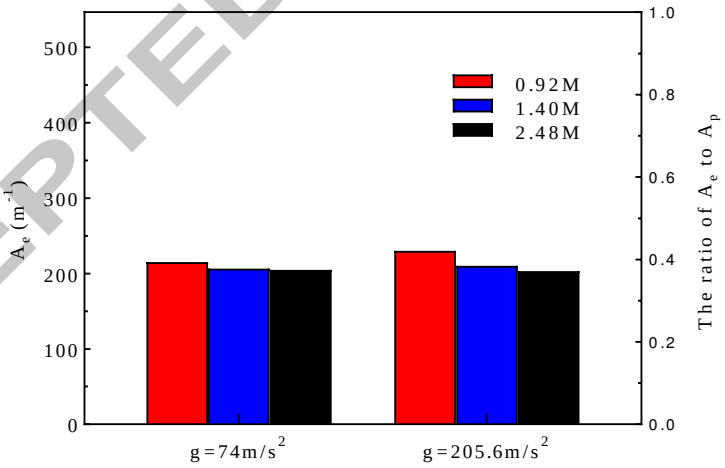

Fig. 5. Predicted effective interfacial area using three different grids.

Table 3. Grid convergence study for A_e at g=74 m/s^2 and g=205.6 m/s^2.

	R_K	δ_{RE}	P	δ	U_G (%)
g=74 m/s^2	0.16	0.16	5.82	0.96	3.42%
g=205.6 m/s^2	0.34	2.08	3.81	7.92	26.07%

3.2. Comparing CFD results with experimental data

In order to validate the CFD model then further experiments need to be undertaken for observing the liquid flow in the expanded stainless steel mesh packing under a centrifugal force. However, due to the strong limitations in the experimental measurements in the RPB when it is rotating, the CFD model validations are performed under the force of gravity. Fig. 6 depicts a schematic diagram of the experimental setup. Two pieces of tightly bound mesh sheets, supplied by The Expanded Metal Company in the UK are vertically fixed on a support, and the texture of the mesh is perpendicular to each other and this is the same as the arrangement of the mesh in the simulation. The liquid is supplied to the mesh from ten evenly distributed nozzles with 1 mm diameter, which are placed vertically above the mesh. The liquid flow rate is controlled by adjusting the liquid level in the tank over the mesh sheets. Several overflow drains are installed on the tank and the liquid level can be controlled at different heights by opening the different overflow drains. The liquid flow rate is measured by calculating the difference in the flow rates between the supply tank and the collecting tank. Water and 70 wt% glycerol solution are used in the experiments. In order to increase the visibility of the liquid when it flows through the mesh sheets, a small amount of blue ink (less than 2%) is added to the water. Due to the amount of blue ink being very small, its effect on the physical properties of the liquids is negligible. The experiments are carried out at ambient pressure (~1 atm) and room temperature (~20 °C). The properties of the liquids are listed in Table 2. A digital camera (Casio Exilim F1, Japan) with the maximum speed of 60 frames per second and the maximum resolution of 6 million pixels is used to capture the details of the liquid flow by focusing on a small region of the mesh sheets as illustrated in Fig. 6.

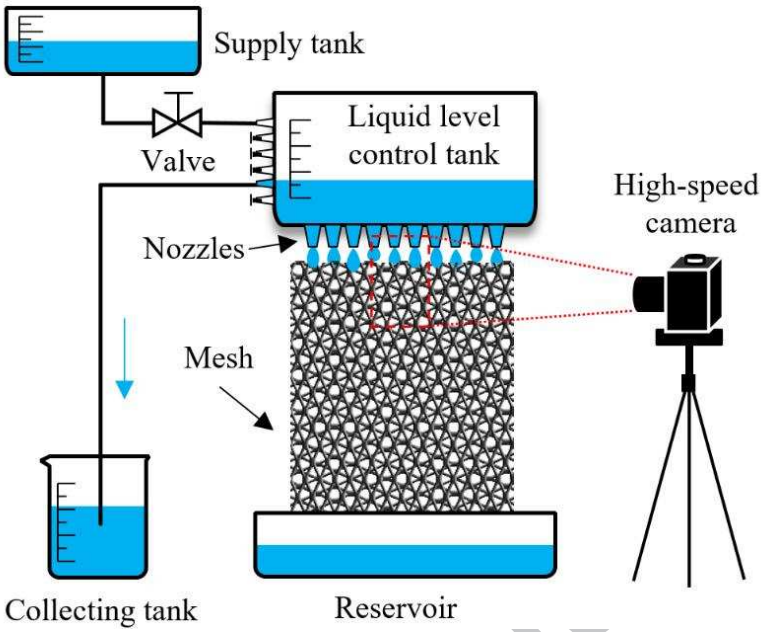

Fig. 6. Schematic diagram of the experimental setup.

Numerical simulations of the flow through the REU have been compared with experimental observations under gravitational conditions and with the same liquid flow rates. Fig. 7(a1) and (a2) show the water flowing in the mesh packing obtained by the simulation and experimental methods, respectively. Fig. 7(b1) and (b2) show the 70 wt% glycerol aqueous solution, which has a higher viscosity than water, flowing in the mesh packing. In both cases, the liquids are released from two nozzles with 1 mm diameter above the packing region and the jet velocity is controlled at 0.5 m/s. It is clearly observed that both the water and the glycerol solution flows through the interspace of the packing, which can be classified as the pore flow. However, the high viscosity of the glycerol solution reduces the liquid velocity and increases the thickness of the liquid films on the packing surface, and thus there is more glycerol solution held on the packing. Further, for performing a quantitative comparison between the CFD simulations and the experimental results, the characteristic liquid holdup, which is defined as the fraction of the liquid phase area to the total packing unit area from the photographic shooting direction is compared. The characteristic liquid holdup is obtained through processing the experimental snapshots and the contours of the liquid from the CFD simulations. For the experimental snapshots, due to the liquid being dyed by blue ink, the liquid phase area is identified by recognising the pixels in the blue colour. From the statistical point of view, the characteristic liquid holdup can reflect the amount of actual liquid holdup. The average characteristic liquid holdup over a period of time are shown in Fig. 8. The experimental uncertainties are

based on the standard deviation of the observed results. It shows that the characteristic liquid holdup from the CFD simulations is approximately the same as those obtained from the experimental results. This demonstrates that the CFD model has a reasonable accuracy to simulate the liquid flow in the packings with complicated structures. It is worth mentioning that, in the future, further validations of the CFD model under centrifugal fields should be performed based on improved experimental measurement technologies.

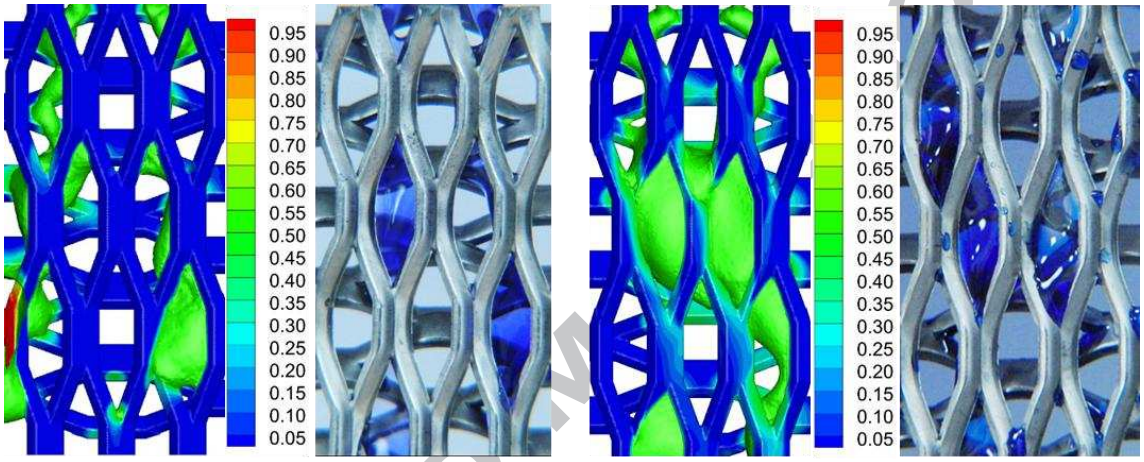

Fig. 7. Liquid flow patterns in the expanded mesh packings: (a1) CFD simulation and (a2) experimental snapshot with water flow, v=0.5m/s, and (b1) CFD simulation and (b2) experimental snapshot with 70% glycerol, v=0.5m/s (VOF=0.5 is regarded as the gas/liquid interface).

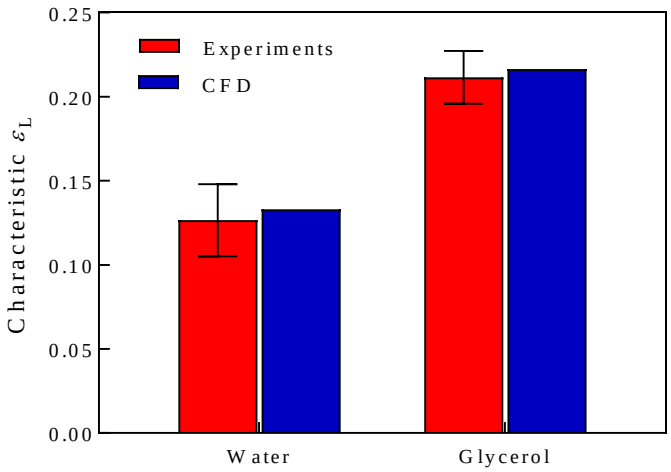

Fig. 8. Comparison of the CFD simulation results of the average characteristic liquid holdup with the experimental data.

3.3. Effect of the liquid inlet configuration

In order to assess the configuration of the liquid inlet on the liquid distribution in the REU, different numbers of evenly distributed nozzles with the same total liquid flow rate and the same diameter are investigated. The diameter of the nozzle is set as 1 mm, which is close to the diameter of the droplets in the RPB as observed in the experiments (Sang et al., 2017) and the number of nozzles tested ranges from 5 to 14. The calculation domain is divided evenly into 6 regions along the radial direction from the liquid inlet boundary to the outlet boundary. The average liquid holdup (ε_L) and average specific surface area of the liquid (A_s) in each region are shown in Fig. 9(a) and Fig. 9(b), respectively. Close to the liquid inlet nozzles, ε_L is the highest among all the regions and then it dramatically decreases in the second region. This is because the liquid impinges on the packing in the first region and accumulates here, and then it speeds up quickly under the centrifugal force. After a short distance, the centrifugal force is in balance with the drag force from the packing, and then the average speed of the liquid is almost constant. After impinging on the packing, the liquid is dispersed, and therefore A_s keeps increasing in the region that is close to the liquid entrance, as shown in Fig. 9(b). However, the liquid dispersion develops into a steady state within a short distance, therefore A_s remains almost constant in the region that is 15.81 mm away from the liquid entrance. Therefore, the flow patterns and data discussed in Section 4 are obtained from the region that is 15.81 mm away from the liquid entrance, which is half of the REU region away from the liquid inlet. In addition, with the increasing number of nozzles, the liquid holdup increases due to the decreasing liquid initial velocity, however, the increase in the liquid holdup becomes small when the number of nozzles is more than 12. Therefore, the nozzle number is set as 12 in the following investigations.

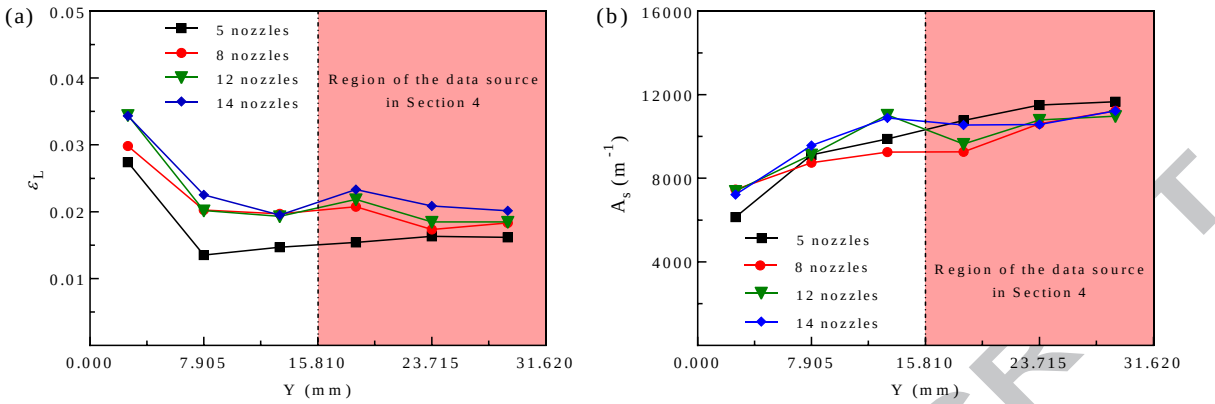

Fig. 9. Effect of the liquid inlet configuration on the on the liquid distribution along the radial direction in the REU: (a) Liquid holdup (ε_L) and (b) specific surface area of the liquid (A_s) (g=205.6 m/s^2, U=0.0106m/s, 50 wt% MEA, $\gamma = 75°$).

4. Results and discussion

4.1. Liquid flow patterns in the REUs

The simulated profiles (including the front, right and back views) of the liquid flows in the mesh packing with different centrifugal accelerations, liquid loads and viscosities are shown in Fig. 10. Generally, the liquids that flow in the interspace of the packing are mainly in the form of films, ligaments and droplets, which are similar to the experimental observations (Burns and Ramshaw, 1996; Guo et al., 2000; Zhang et al., 2000). In addition, more liquid is attached to the longitudinal wires than the latitude wires in general. Further, the dynamic behaviour of the liquid in the RPB can be observed in the simulations, where the liquid film that attaches on the packing surface flows radially under the action of the inertial centrifugal force. When the direction of the wire is not aligned with the inertial centrifugal force, the liquid film has a trend to move away from the packing surface, and if the inertia of the film is strong enough to overcome the adhesive force from the packing, the liquid will separate from the packing surface and form droplets. Then, the free droplet will hit the wires downstream of the current wire and form a liquid film. The above dynamic process is repeated in the packing region, which promotes the surface renewal of the liquid and this is advantageous for the gas-liquid mass transfer. In addition, due to the direction of the latitude wires being perpendicular to the inertial centrifugal force, more droplets are detached from the latitude wires than the longitudinal wires. Therefore, a larger percentage of the latitude

wires leads to a larger percentage of droplets in the RPB, and a larger percentage of longitudinal wires generates more liquid films. However, it is worth mentioning that the influence of the packing structure and layout on the flow patterns still requires further investigations, and the use of the mesoscale CFD modelling method is a good way to perform the investigations.

In addition, the effects of the operating parameters and liquid properties on the flow patterns have been investigated. For example, the effect of centrifugal acceleration g on the liquid flow pattern can be directly observed through comparing Fig. 10(a) and (b), where the values of the centrifugal acceleration are 74.0 and 205.6 m/s^2, respectively. As shown in Fig. 10(a), at a small centrifugal field (74.0 m/s^2), the liquid is mainly in the state of thick liquid films that attach on the packing surface. Then, with the increasing of g, as shown in Fig. 10(b), the liquid films become elongated and thinner and the droplets become smaller. The effect of liquid load on the liquid flow pattern can be observed from comparing Fig. 10(a) and (c), where the values of the liquid superficial velocity (U) are 0.0106 and 0.0159 m/s, respectively. As can be seen, the liquid flow patterns are similar but the liquid volume increases with increasing U. On comparing Fig. 10(b) and (d), the effect of MEA concentration on the liquid flow pattern can be observed. The 90 wt% MEA, with a higher viscosity results in the thicker liquid films on the packing surface and the wetted wall area is larger than that of the 50 wt% MEA.

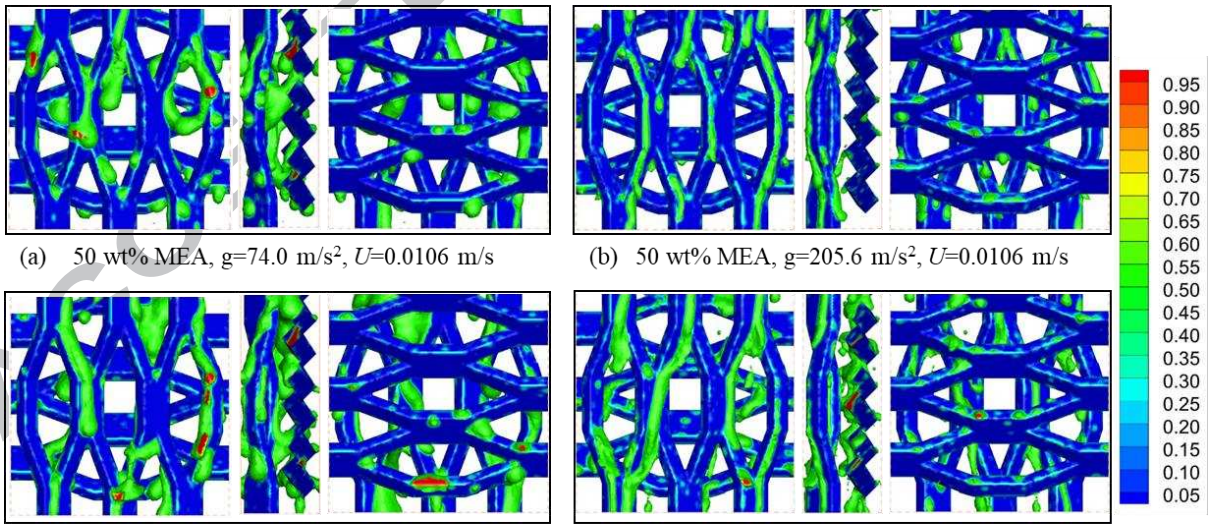

(a) 50 wt% MEA, g=74.0 m/s², *U*=0.0106 m/s (b) 50 wt% MEA, g=205.6 m/s², *U*=0.0106 m/s

(c) 50 wt% MEA, g=74.0 m/s², *U*=0.0159 m/s (d) 90 wt% MEA, g=205.6 m/s², *U*=0.0106 m/s

Fig. 10. Liquid flow patterns in the REU at different conditions (γ=75°).

4.2. Characteristic parameters of the liquid flow in the REU

4.2.1 Definition of the characteristic parameters

Characteristic parameters are very helpful in characterising the liquid flow in the REU. Several important parameters, such as liquid holdup (ε_L), volume fraction of the droplets (F_d), effective interfacial area (A_e), wetted wall area (A_w), and specific surface area of the liquid (A_s), are defined in this section.

The liquid holdup (ε_L) is an essential parameter for gas-liquid reactors (Basic and Dudukovic, 1995). In the REU, it is defined as follows:

$$\varepsilon_L = \frac{V_l}{V_p} \tag{8}$$

where V_l is the liquid volume in the data source region of the REU (ref. Fig. 9), and it is obtained through integrating the volume fraction of the liquid phase in each cell; V_p is the packing volume of the data source region in the REU, which includes the volume occupied by the porous packing material and the flow space.

The films that attach on the packing surface have very different flow dynamics and mass transfer mechanisms from the detached droplets. Therefore, distinguishing the droplets from the films in the REU is important for establishing an accurate mass transfer model, and the volume fraction of the detached droplets (F_d) is defined as follows:

$$F_d = \frac{V_d}{V_l} \tag{9}$$

where V_d is the volume of the detached droplets in the data source region of the REU.

The simulations are performed in two steps to calculate V_d. In the first step, the time-dependent computation is conducted until the flow achieves a pseudo-steady state. Then, the mass transfer simulation is performed by setting a tracer concentration boundary condition on the packing surface and solving a convective-diffusive equation to make the tracer diffuse in the liquid films that are attached to the packing surface until the simulation reaches the quasi-steady state. In this way, the liquid films that are in contact with the packing surface are marked by the tracer concentration, while the detached liquids that are mainly in the form of droplets are not marked by the tracer concentration. Further, V_d is calculated by integrating the volume of liquid that is not marked by the tracer concentration. It is worth noting that some droplets may also be in contact with the packing surface and the tracer may cause an unpredictable error.

The effective interfacial area (A_e), which is used for calculating the mass transfer and gas-liquid drag force, is defined as follows:

$$A_e = \frac{A_{g-l}}{V_p} \tag{10}$$

where A_{g-l} is the gas-liquid interfacial area in the data source region of the REU, and it is calculated through integrating the gas-liquid interfacial area in each cell (a_{g-l}) of the data source region in the REU. From the viewpoint of CFD (ANSYS Inc, 2016), a_{g-l} is calculated by using the gradient of the volume fraction in each computational cell as follows:

$$a_{g-l} = |\nabla \alpha_l| = |\nabla \alpha_g| \tag{11}$$

which has been used to calculate the gas-liquid interfacial area in the VOF models (Sebastia-Saez et al., 2015b; Xu et al., 2009).

In addition, the wetted wall area (A_w), which is an important parameter for predicting the drag force between the packing and the liquid, is defined as follows:

$$A_w = \frac{A_{l-s}}{V_p} \tag{12}$$

where A_{l-s} is the liquid-solid interfacial area in the data source region of the REU.

The specific surface area of the liquid (A_s) can be used to assess the degree of liquid dispersion, and it is defined as follows:

$$A_s = \frac{A_{g-l}}{V_l} = \frac{A_e}{\varepsilon_L} \tag{13}$$

All the original data for calculating these parameters are accessed through writing UDFs.

4.2.2 Effect of the centrifugal acceleration

The centrifugal acceleration g in an RPB changes with the rotational speed ω and the radial position r of the RPB. 50 wt% MEA, with a nominal viscosity of 3.35 mm^2/s, is used for simulating the typical liquid flow in an RPB for CO_2 capture. The effect of the centrifugal acceleration g on the liquid holdup ε_L is examined for two liquid flow rates and the superficial velocities are 0.0053 m/s and 0.0106 m/s, respectively, which are within the typical operational conditions of the RPB. The variation of ε_L is shown in Fig. 11(a). On increasing g from 32.9 to 296.1 m/s^2, ε_L keeps decreasing, but the downtrend gradually becomes weaker after 150 m/s^2. Variation of the droplet holdup and the volume fraction of the droplets F_d with the increasing of g are shown in Fig. 11(b). On increasing g, the inertia of the liquid increases and therefore more liquids are stripped from the packing surface and turn into the detached droplets. Fig. 11(c) shows the effect of g on the variation of the effective interfacial area A_e and the wetted wall area A_w. It is

observed that A_e slightly increases but A_w slightly decreases with the increasing of g. The slightly increasing of A_e is the composite effect of decreasing the liquid holdup but increasing the liquid dispersion (see Fig. 11 (a) and (d)). While, the slightly decreasing of A_w could be due to some liquid films changing into detached droplets. From the right Y-axial of Fig. 11(c), it is observed that A_e and A_w only take 30-40% and 10-20% of the specific surface area of the packing A_p, respectively. This demonstrates that A_e and A_w are not recommended to be regarded as A_p in the mass transfer calculations. Fig. 11(d) indicates that the specific surface area of the liquid A_s keeps increasing when g changes from 32.9 to 296.1 m/s^2. Due to the change of A_e being very little with the increase in g, the increasing of A_s is mainly due to the reduced ε_L.

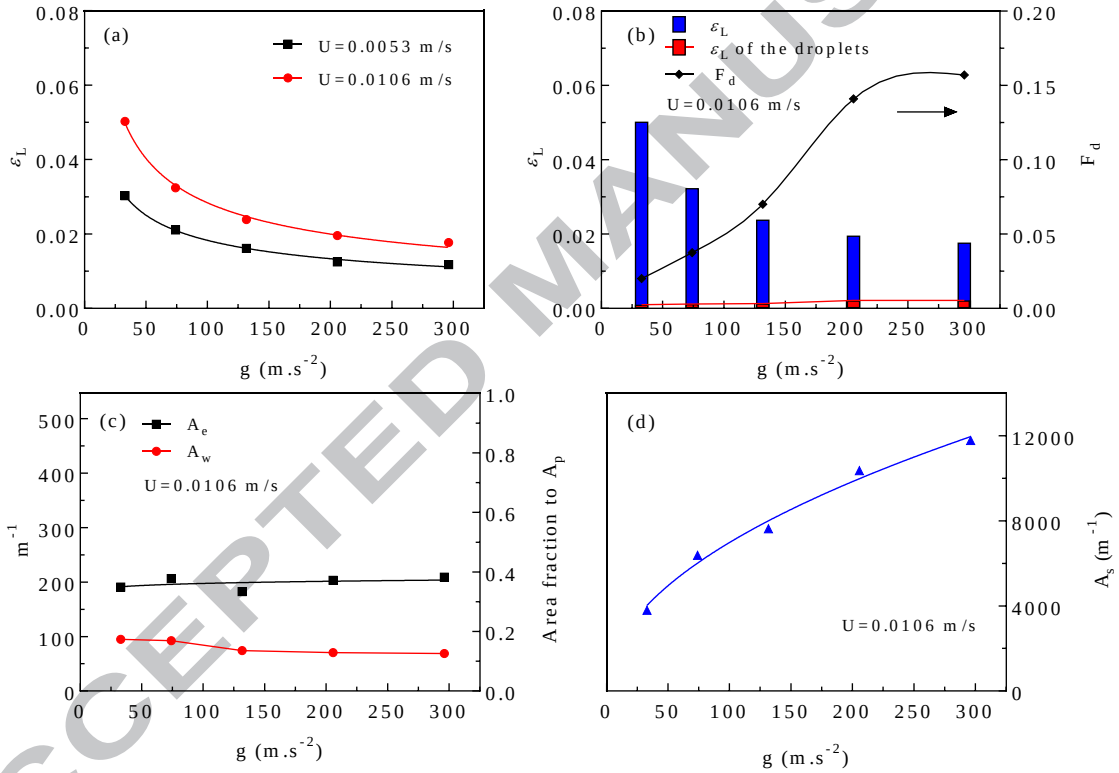

Fig. 11. Effect of g on the characteristic parameters of the liquid flow in the REU: (a) liquid holdup ε_L, (b) volume fraction of the droplets F_d, (c) effective interfacial area A_e and wetted wall area A_w, and (d) specific surface area of the liquid A_s. (50 wt% MEA, $\gamma = 75°$)

4.2.3 Effect of the liquid load

According to Eq. (1), the liquid superficial velocity U in an RPB changes with the liquid flow rate Q and the radial position r of the RPB. The effect of U on the liquid flow characteristics is examined with g at 74.0 m/s^2 and 205.6 m/s^2 respectively, and the liquid is set as the 50 wt% MEA. As shown in Fig. 12(a),

ε_L increases with the increase in U from 0.0053 m/s to 0.0159 m/s, and the growth rate is higher at a lower g. In addition, Fig. 12(b) shows that both A_e and A_w increase with increasing U. Due to the increasing rate of ε_L being larger than the increasing rate of A_e at the same g, the specific surface area of the liquid A_s decreases with the increasing U, as shown in Fig. 12(c). This means that the degree of liquid dispersion decreases with increasing U.

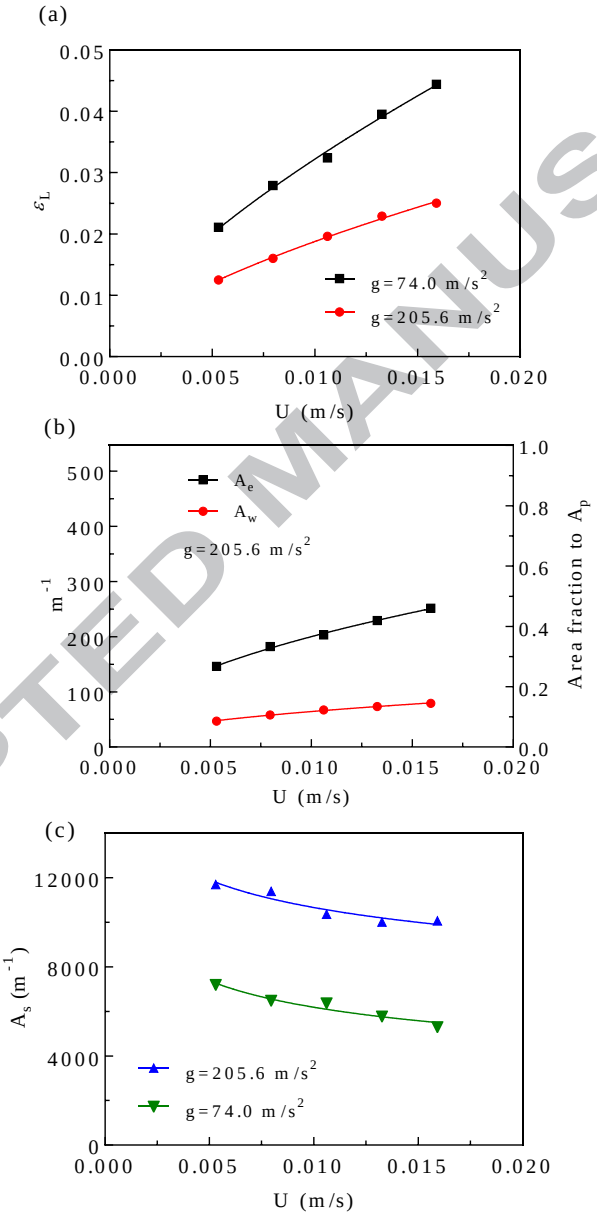

Fig. 12. Effect of U on the characteristic parameters of the liquid flow in the REU: (a) liquid holdup ε_L, (b) effective interfacial area A_e and wetted wall area A_w, and (c) specific surface area of the liquid A_s. (50 wt% MEA, $\gamma = 75°$, the gas inlet velocity is set as 20% of the liquid inlet velocity)

4.2.4 Effect of the liquid viscosity

With the increasing of the MEA concentration, the viscosity correspondingly increases and it has a large influence on the liquid flow in the RPB. The effect of the liquid viscosity (ranging from 1.66 mm^2/s to 10.12 mm^2/s) on ε_L and the volume fraction of the droplets F_d is shown in Fig. 13(a) and (b) respectively, which corresponds to the MEA concentration increasing from 30 wt% to 90 wt%. ε_L increases with the increasing viscosity, but F_d decreases. This is mainly due to the increase in the thickness of the liquid film and the decrease in the velocity of the liquid flow. In addition, if droplets strip from the liquid film, they have to overcome a greater viscous force. From Fig. 13(c) and (d), both A_e and A_w slightly increase with the increasing viscosity, while A_s decreases with the increasing viscosity at the same g. This suggests that the increasing viscosity can weaken the liquid dispersion. Due to A_s being larger at a higher g, as shown in Fig. 13(d), increasing g could be a solution for increasing A_s when dealing with a high viscosity liquid.

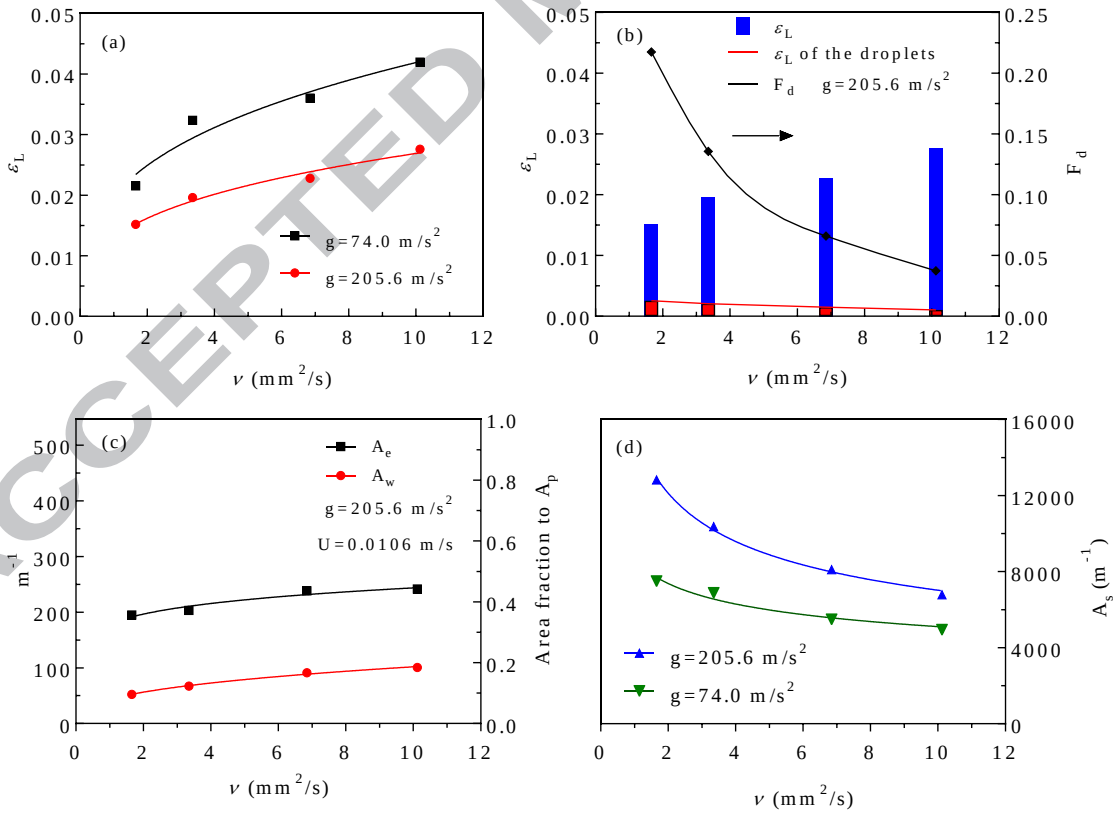

Fig. 13. Effect of liquid viscosity on the characteristic parameters of the liquid flow in the REU: (a) liquid holdup ε_L, (b) volume fraction of the droplets F_d, (c) effective interfacial area A_e and wetted wall area A_w, and (d) specific surface area of the liquid A_s. (U=0.0106 m/s, $\gamma = 75°$)

4.2.5 Effect of the contact angle

The contact angle γ of the packing surface is a sensitive parameter for influencing the liquid flow morphology and it further influences the mass transfer performance in a gas-liquid reactor (Sebastia-Saez et al., 2018). Stainless steel is usually hydrophilic but γ is variable with different surface treatments (Zhang et al., 2017). In order to cover wide properties of the packing materials, the effect of γ ranged from 30° to 150° on the liquid flow characteristics is investigated. Fig. 14 shows the liquid flow pattern in the REU for different values of γ. It demonstrates that the liquid flow pattern gradually changes from the film-dominated flow to the droplet-dominated flow with increasing of γ. This trend also can be obtained from Fig. 15(b), where the volume fraction of the droplets increases with increasing γ. However, ε_L reduces with increasing γ, as shown in Fig. 15(a). This is because the packing has a weaker resistance to the droplets than films, and this makes the droplets have much higher velocities than the films. From Fig. 15(c), A_e and A_w decrease with the increasing γ. The decreasing of A_e is partly due to the decrease in liquid holdup. The decreasing of A_w is mainly due to the less wettability of the surface with increasing γ. In addition, as shown in Fig. 15(d), A_s increases with increasing γ, and this is mainly because the liquid is easier to break into small droplets with a hydrophobic surface, which also has been observed in the experiments of Zheng et al. (2016) and Zhang et al. (2017). Moreover, a higher g combined with a higher γ further promotes the breakup of the liquid.

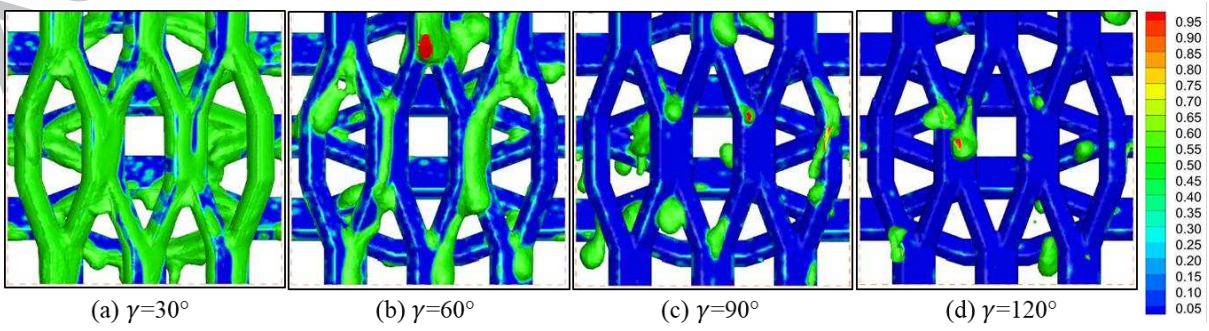

(a) γ=30° (b) γ=60° (c) γ=90° (d) γ=120°

Fig. 14. Simulated profiles of the liquid flows in the mesh packing with different contact angles (50 wt% MEA, g=74.0 m/s^2, U=0.0106 m/s).

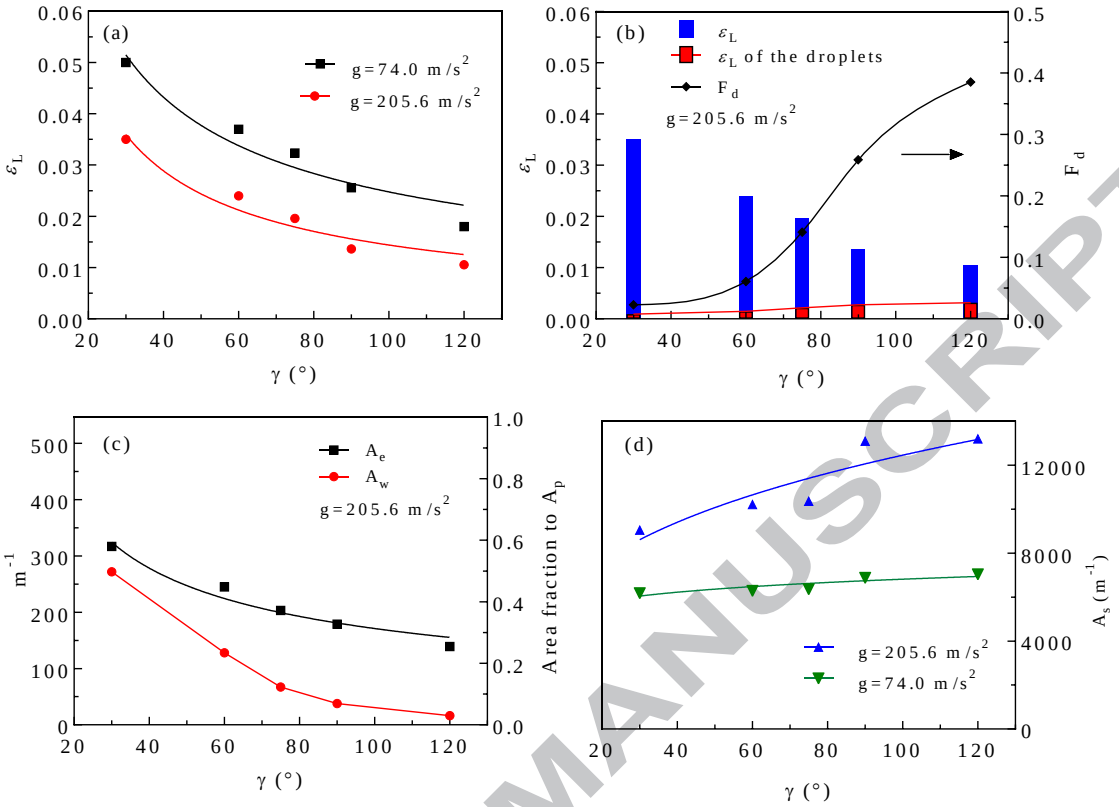

Fig. 15. Effect of contact angle on the characteristic parameters of the liquid flow in the REU: (a) liquid holdup ε_L, (b) volume fraction of the droplets F_d, (c) effective interfacial area A_e and wetted wall area A_w, and (d) specific surface area of the liquid A_s. (50 wt% MEA, U=0.0106 m/s)

4.3. Correlations for ε_L, A_e and A_s

4.3.1 Correlations from the CFD simulation data and validations

Several correlations for the liquid holdup ε_L (Basic and Dudukovic, 1995; Burns et al., 2000; Lin et al., 2000; Yang et al., 2015a) and the effective interfacial area A_e (Luo et al., 2012; Luo et al., 2017; Rajan et al., 2011) in RPBs have been proposed. These correlations are mainly obtained using mathematical regression based on numerous sets of experimental data from certain RPBs and at certain operating conditions. However, the effect of the contact angle on the hydrodynamic parameters of the RPB has not been considered in the existing correlations. In addition, there are no correlations regressed from RPBs with the expanded stainless steel mesh packing and no correlations that focus on the concentration range of the MEA solutions that aimed at CO_2 capture. Due to lack of experimental data at these conditions, generating correlations from CFD simulation data could be an effective and economical alternative to meet

the requirement of accurate prediction of the performance of the RPB for CO_2 capture. Among the existing correlations, the Burns correlation (Burns et al., 2000) describes the relationship between liquid holdup (ε_L) and the centrifugal acceleration (g), liquid superficial velocity (U) and viscosity (ν), which is concise and clear, and it has been adopted in many cases (Joel et al., 2015; Joel et al., 2014, 2017; Kang et al., 2014; Thiels et al., 2016). Therefore, a similar expression has been adopted to regress the correlations for ε_L, A_e and A_s in the RPB with an expanded mesh packing based on the CFD simulation results. Due to the contact angle having a large influence on these parameters, it has been taken into account in this model as follows:

$$y = a\left(\frac{g}{g_0}\right)^m \left(\frac{U}{U_0}\right)^q \left(\frac{\nu}{\nu_0}\right)^n \left(\frac{\gamma}{\Upsilon_0}\right)^p \tag{14}$$

where $g_0 = 205.6\ \mathrm{m/s^2}$, $U_0 = 0.0106\ \mathrm{m/s}$, $\nu_0 = 3.35\ \mathrm{mm^2/s}$, $\Upsilon_0 = 75°$ are the characteristic values for g, U, ν and γ in a typical operating condition. y is ε_L, A_e or A_s, and a, m, q, n, and p are the coefficients to be obtained from the regression analysis. First, this exponential function is transformed into a linear function through the logarithm operation; then the least squares regression (LSR) method is used for the regression analysis due to the weak collinearity among the independent variables (Wang, 1999; Yang et al., 2017).

The regression equations are given as follows, which are based on the 31 sets of data gathered from the CFD simulations, and the data are provided in the supplementary materials.

For the liquid holdup:

$$\varepsilon_L = 0.0188\left(\frac{g}{g_0}\right)^{-0.4764} \left(\frac{U}{U_0}\right)^{0.5716} \left(\frac{\nu}{\nu_0}\right)^{0.3197} \left(\frac{\gamma}{\Upsilon_0}\right)^{-0.7557} \tag{15}$$

For the effective interfacial area:

$$A_e = 202.3485\left(\frac{g}{g_0}\right)^{0.0435} \left(\frac{U}{U_0}\right)^{0.4275} \left(\frac{\nu}{\nu_0}\right)^{0.1200} \left(\frac{\gamma}{\Upsilon_0}\right)^{-0.5856} \tag{16}$$

For the specific surface area of the liquid:

$$A_s = 10517.1970\left(\frac{g}{g_0}\right)^{0.4946} \left(\frac{U}{U_0}\right)^{-0.1515} \left(\frac{\nu}{\nu_0}\right)^{-0.2921} \left(\frac{\gamma}{\Upsilon_0}\right)^{0.1658} \tag{17}$$

The availability of these correlations to predict ε_L, A_e and A_s at different radial positions of an RPB are examined. This is achieved through comparing the predicted results from the correlations with the new CFD simulation results, which are obtained by setting the REU at four radial positions (r=0.11, 0.3, 0.38, 0.49 m) with three rotational speeds (N=150, 250, 300 rpm). The examination is conducted at the liquid flow rate of 14.4 m^3/h, and 50% MEA are used as the liquid phase and the contact angle is set as 75°. The

test data are provided in the supplementary materials. From Fig. 16 (a1), (b1) and (c1), it can be seen that the correlations have a good performance to predict ε_L, A_e and A_s with the radial position ranging from 0.1 to 0.5 m. Further, both the 31 sets of training data and the 9 sets of test data of ε_L, A_e and A_s are displayed in Fig. 16(a2), (b2) and (c2), and most of the data lie within ± 20% of the values predicated by Eq. (15), (16) and (17), respectively. This demonstrates that the correlations are valid to predict ε_L, A_e and A_s at different radial positions of an RPB.

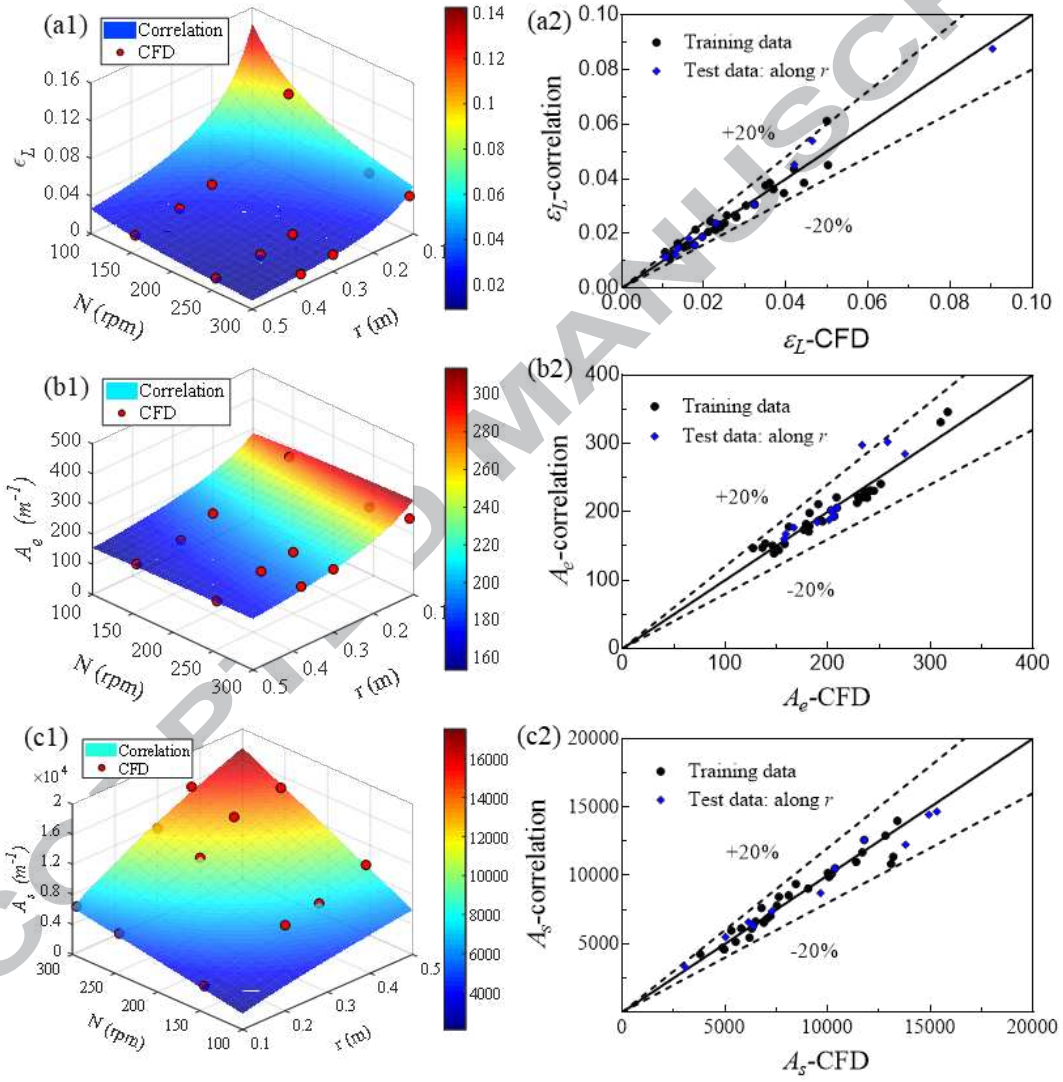

Fig. 16. Comparison of the characteristic parameters between the predicted values from the correlations and CFD: (a) liquid holdup ε_L, (b) effective interfacial area A_e and (c) specific surface area of the liquid A_s.

In order to further validate the proposed correlation, the exponents m, q, n of the corresponding independent variables g, U, ν in the ε_L correlation Eq. (15) are compared with those obtained in previous

investigations, including the exponents in the Basic and Dudukovic correlation (Basic and Dudukovic, 1995), Burns correlation (Burns et al., 2000) and two theoretical models (Burns et al., 2000), as listed in

Table 4. From the theoretical model that is summarised in Burns et al. (2000), there are two extreme flow models: viscous flow and inertial flow. In the case of viscous flow, the liquid is assumed to flow as fully developed laminar films over the packing surface, then m= -0.33, q= 0.33 and n= 0.33. In the case of inertial flow, the kinetic energy of the flow is mainly lost by the frequent collisions with the packings, and it includes inertial film flow, pore flow and droplet flow, then m= -0.5, q= 1, n= 0. As can be seen in

Table 4, the value of the exponents m, q and n that are derived from the CFD data are located between the limits of the two theoretical models. The absolute value of m is smaller but n is larger than the corresponding values in the Burns correlation, which suggests that there are more viscous film flows in the current investigation than in the investigation of Burns et al. (2000). This is probably caused by the different packing structures and different void fractions. The expanded stainless steel mesh packing is used in this paper while the reticulated foam packing is used in the experiments of Burns, and the void fraction (ε) of the packing that is used in this paper (0.84) is smaller than that in the experiments of Burns (0.953). In addition, the exponents from the current investigation are within the limits of the exponents from the experiments of Basic and Dudukovic (1995), which used glass beads packings with lower void fractions (0.348 and 0.466). The comparisons between the different investigations indicates that the essential flow mode should be similar in the RPBs, although the sensitivity of the investigated parameters that influence ε_L is different for different packing structures and void fractions. The exponent of p for predicting the effect of the contact angle (γ) appears to be very important for influencing ε_L, but it has not been investigated in the previously mentioned investigations. Further, the new proposed correlation (Eq. (15)) has been used to predict the ε_L in the experiments of Burns et al. (2000) and Yang et al. (2015a). The experimental data of ε_L and the ε_L predicted by Lu model (Lu et al., 2018) and the new proposed correlation (Eq. (15)) are plotted in Fig. 17 (a) and (b). It is observed that the predicted ε_L is close to the experimental data and the predictions of the Lu model.

Table 4 Comparison of the exponents m, q, n and p for ε_L.

Data Source	Packing type	m (of g)	q (of U)	n (of ν)	p (of γ)
ε_L-CFD	Expanded stainless steel mesh packing (ε=0.84)	-0.4764	0.5716	0.3197	-0.7557
ε_L-Theoretical inertial model		-0.5	1.0	0	--
ε_L-Theoretical viscous model		-0.33	0.33	0.33	--
ε_L-Burns	Reticulated foam (ε=0.953)	-0.5	0.6	0.22	--
ε_L-Basic and Dudukovic	Glass beads (ε=0.348, 0.466)	-0.48 ~ -0.36	0.57 ~ 0.64	0.23 ~ 0.51	--

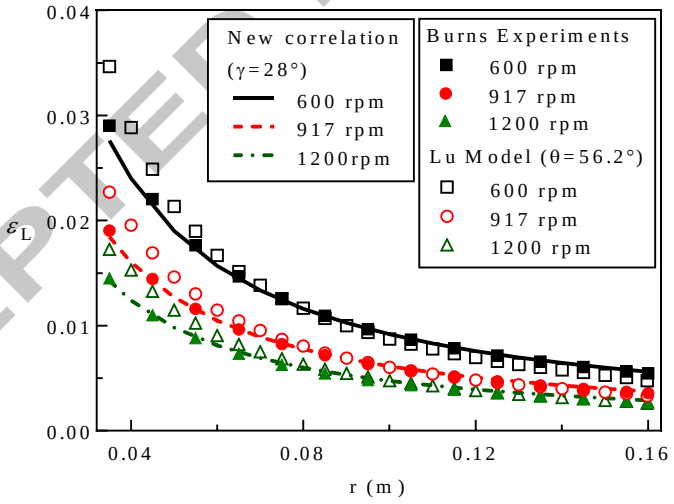

(a)

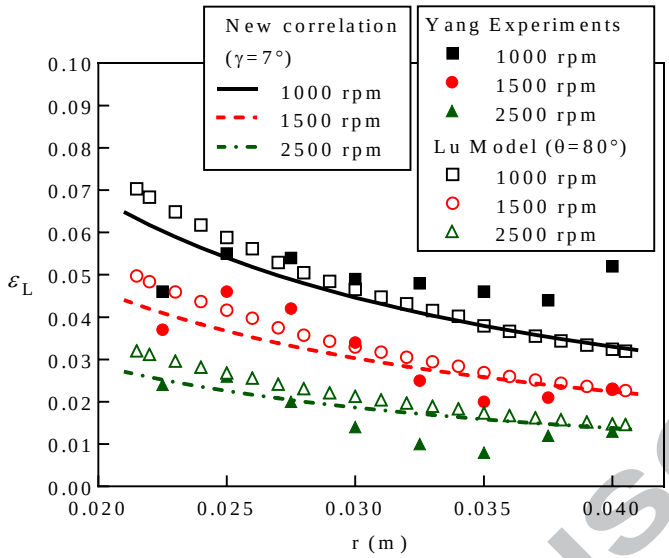

(b)

Fig. 17. Comparison of the ε_L between the new correlations, experimental data and existing model (Lu et al., 2018): (a) Burns case (Q_L=1.75*10^{-5} m^3/s) (Burns et al., 2000) and (b) Yang case (Q_L=2.29*10^{-5} m^3/s) (Yang et al., 2015a).

4.3.2 Practical implications of the correlations

In order that the correlations explicitly connect to the practical operations, the centrifugal acceleration g is decomposed into the radial position r and the rotational speed ω based on the following equation:

$$g = r\omega^2 \tag{18}$$

Therefore, on substituting Eq. (1) and Eq. (18) into Eq. (14), then Eq. (14) becomes:

$$y = E\omega^{2m} {Q_L}^q r^{(m-q)} \nu^n \gamma^p \tag{19}$$

where E is an empirically derived constant.

The independent variables in Eq. (19) cover most of the important parameters in the operation and design of an RPB. For example, ω and Q_L are the main operating parameters and both of them are highly relevant to the operating cost in the CO_2 capture process. Further, r is the important structural parameter that is relevant to the volume and weight of the bed, ν is the physical property of the solvents that flows in the RPB, and γ is the property of the packing materials. Therefore, analysing the exponents of these parameters has very important practical implications.

Table 5 lists the exponents of ω, Q_L, r, ν and γ for predicting ε_L, A_e and A_s. A positive exponent means the dependent variable has a positive correlation with the independent variable, and vice versa. In addition,

the absolute value of an exponent represents the sensitivity of the dependent variables to the change in the corresponding independent parameters.

Table 5 Comparison of the exponents ω, Q_L, r, ν and γ for predicting ε_L, A_e and A_s.

Parameters	2m (of ω)	q (of Q_L)	m-q (of r)	n (of ν)	p (of γ)
ε_L	-0.9528	0.5716	-1.048	0.3197	-0.7557
A_e	0.0870	0.4275	-0.384	0.1200	-0.5856
A_s	0.9892	-0.1515	0.6461	-0.2921	0.1658

(i) For the liquid holdup ε_L, the exponents of Q_L, ν are positive, and the exponents of ω, r and γ are negative, in addition, the sensitivity of the independent variables is ranked as follows: $r > \omega > \gamma > Q_L > \nu$. This means that the viscosity ν is the weakest parameter while the radial position r is the strongest parameter for influencing ε_L. Moreover, the exponent of r is approximately -1, which means ε_L almost reduces inversely proportional to the local packing radius in an RPB. Therefore, for the scale up design of an industrial scale RPB for CO_2 capture, the radial thickness of the rotating packed bed should not be too large in order to prevent the severe liquid maldistribution along the radial direction in the RPB. In addition, enlarging the RPB in the axial direction or the design of RPBs with multistage liquid nozzles along the radial directions could be the feasible solutions.

(ii) For the effective interfacial area A_e, the exponents of ω, Q_L and ν are positive, and the exponents of r and γ are negative. In addition, the sensitivity of the independent variables is ranked as follows: $\gamma > Q_L > r > \nu > \omega$. This indicates that within the investigation conditions in this paper, in order to increase A_e, decreasing the contact angle γ could be the most effective option, while increasing the rotational speed ω is the most inefficient way. Therefore, a high rotational speed is not recommended in order to achieve a large A_e by both considering the performance of the RPB and the energy consumption for driving the RPB.

(iii) For the specific surface area of the liquid A_s, the exponents of ω, r and γ are positive, and the exponents of Q_L and ν are negative. The sensitivity of the independent variables is ranked as follows: $\omega > r > \nu > \gamma > Q_L$. This indicates that increasing ω is the most effective way to increase A_s.

In addition optimizing a single characteristic parameter, multiple characteristic parameters should be considered for optimizing a particular application of the RPB. From the aspect of CO_2 absorption

(Uchiyama et al., 2003), increasing A_e is the first choice to facilitate the CO_2 absorption rate in the RPB. According to the correlation for A_e, both increasing Q_L and decreasing γ are two effective solutions to increase A_e. However, both of the two solutions have negative impacts on A_s, which reduces the utilization efficiency of the solvents. Due to A_s being very sensitive to ω, an appropriate increase in ω could reduce the side effects of increasing A_e which resulted from the increase in Q_L and the decrease in γ. In addition, using high-concentrated MEA aqueous solutions has good potential to reduce the volume ratio of the solvents to CO_2, which can reduce the energy consumption in MEA regeneration. However, the increasing viscosity ν decreases A_s, which could decrease the utilization efficiency of MEA. Therefore, increasing ω and/or increasing γ appropriately are possible solutions to deal with this issue through analyzing the exponents.

5. Conclusions

This paper proposes a new mesoscale 3D CFD model to investigate the liquid flow characteristics in the RPB. The model has been validated through comparing the results obtained with experimental observations. Detailed liquid flow patterns, liquid holdup, volume fraction of the droplets, effective interfacial area, wetted wall area and specific surface area of the liquid in the RPB are obtained numerically. The results show that the mesoscale CFD model is effective in analysing the local detailed liquid flow characteristics as well as the overall parameters of an RPB. The main conclusions are as follows:

(i) Increasing the rotational speed dramatically reduces the liquid holdup and increases the specific surface area of the liquid but it has very weak positive effect on increasing the effective interfacial area in the RPB.

(ii) Increasing liquid flow rate and/or increasing liquid viscosity improve both the liquid holdup and the effective interfacial area in the RPB, but they have a negative effect on the specific surface area of the liquid. Higher liquid flow rate and/or higher viscous MEA require higher rotational speed to maintain both the effective interfacial area and the specific surface area.

(iii) The flow pattern, liquid holdup and interfacial area are sensitive to the contact angle. Larger contact angles can generate more liquid droplets with larger specific surface area but the liquid holdup, the

effective interfacial area and the wetted wall area dramatically decrease. Surface modification of the packing is an important method to optimize the mass transfer efficiency in the RPB.

(iv) The correlations for predicting the liquid holdup ε_L, effective interfacial area A_e, and specific surface area A_s in the RPB are proposed. The sensitivities of the investigated effect parameters on ε_L, A_e and A_s respectively are as follows: For ε_L, $r > \omega > \gamma > Q_L > \nu$; For A_e, $\gamma > Q_L > r > \nu > \omega$; For A_s, $\omega > r > \nu > \gamma > Q_L$.

In general, a much better understanding of the liquid flow behaviours within the RPB has been achieved and the factors that influence the mass transfer has been analysed in depth. The proposed model provides a feasible way to predict the hydrodynamic performance of the RPB, which could help to optimize the design and operation of the RPBs.

Acknowledgment

The authors acknowledge the financial support from the EPSRC grants (EP/M001458/2, Process Intensification for Post-combustion Carbon Capture using Rotating Packed Bed through Systems Engineering Techniques) and The Expanded Metal Company for providing the packing samples. P. Xie would like to acknowledge the China Scholarship Council and the University of Sheffield for funding his research studies.

Supplementary materials

Supplementary materials associated with this article can be found in the online version.

Nomenclature

A	entrance area of the REU, m^2
A_e	effective interfacial area, m^{-1}
A_{g-l}	gas-liquid interfacial area in the data source region of the REU, m^2
A_{l-s}	liquid-solid interfacial area in the data source region of the REU, m^2
A_N	total area of the liquid nozzles in the REU, m^2
A_s	specific surface area of the liquid, m^{-1}
A_w	wetted wall area, m^{-1}

a_P	surface area of the packing per unit volume of the bed, m^{-1}
F_d	volume fraction of the droplets
h	thickness of the packed bed, m
k	curvature of the interface
m	exponent of g
N	rotational speed, rpm
n	exponent of ν
$\tilde{n}$	unit normal vector
P	distance metric to the asymptotic range
p	exponent of γ
Q_L	volume flow rate of the liquid, m^3/s
q_L	volume flow rate of the liquid for feeding the REU, m^3/s
q	exponent of U
R_K	convergence ratio
R_i	inner radius of the packing region, m
R_o	outer radius of the packing region, m
r	radial position in the RPB, m
t	time, s
U	liquid superficial velocity, m/s
U_G	grid uncertainty
u_0	liquid inlet velocity in the REU, m/s
V	volume, m^3
V_d	detached droplets volume in the data source region of the REU, m^3
V_l	liquid volume in the data source region of the REU, m^3
V_p	packing volume of the data source region in the REU, m^3
v_r	relative velocity, m/s

Greek symbols

α	volume fraction
γ	contact angle, deg
δ	error estimate
δ_{RE}	error estimate from the Richardson extrapolation method
ε	void fraction of packing

ε_L	liquid holdup
μ	dynamic viscosity, Pa.s
ν	kinematic viscosity, mm^2/s
ρ	density, kg/m^3
σ	surface tension coefficient, N/m
ω	angular speed, rad/s

Subscripts

g	gas phase
l	liquid phase

Abbreviations

CFD	Computational fluid dynamics
FS	Factor of safety
HPC	High performance computing
LFR	Liquid flow rate
LSR	Least squares regression
PCC	Post-combustion capture
PIV	Particle image velocity
REU	Representative elementary unit
RPB	Rotating packed bed
VOF	Volume of fluid

References

Albert, C., Marschall, H., Bothe, D., 2014. Direct Numerical Simulation of interfacial mass transfer into falling films. International Journal of Heat and Mass Transfer 69, 343-357. http://dx.doi.org/10.1016/j.ijheatmasstransfer.2013.10.025.

Amundsen, T.G., Oi, L.E., Eimer, D.A., 2009. Density and Viscosity of Monoethanolamine plus Water plus Carbon Dioxide from (25 to 80) degrees C. Journal of Chemical and Engineering Data 54, 3096-3100. http://dx.doi.org/10.1021/je900188m.

ANSYS Inc, 2016. Theory Guide of ANSYS Fluent 17.2

Basic, A., Dudukovic, M.P., 1995. Liquid Holdup in Rotating Packed-Beds - Examination of the Film Flow Assumption. AIChE Journal 41, 301-316. http://dx.doi.org/10.1002/aic.690410212.

Biliyok, C., Lawal, A., Wang, M.H., Seibert, F., 2012. Dynamic modelling, validation and analysis of post-combustion chemical absorption CO_2 capture plant. International Journal of Greenhouse Gas Control 9, 428-445. http://dx.doi.org/10.1016/j.ijggc.2012.05.001.

Bothe, D., Fleckenstein, S., 2013. A Volume-of-Fluid-based method for mass transfer processes at fluid particles. Chemical Engineering Science 101, 283-302. http://dx.doi.org/10.1016/j.ces.2013.05.029.

Brackbill, J.U., Kothe, D.B., Zemach, C., 1992. A Continuum Method for Modeling Surface-Tension. Journal of Computational Physics 100, 335-354. http://dx.doi.org/10.1016/0021-9991(92)90240-Y.

Burns, J.R., Jamil, J.N., Ramshaw, C., 2000. Process intensification: operating characteristics of rotating packed beds - determination of liquid hold-up for a high-voidage structured packing. Chemical Engineering Science 55, 2401-2415. http://dx.doi.org/10.1016/s0009-2509(99)00520-5.

Burns, J.R., Ramshaw, C., 1996. Process intensification: Visual study of liquid maldistribution in rotating packed beds. Chemical Engineering Science 51, 1347-1352. http://dx.doi.org/10.1016/0009-2509(95)00367-3.

Chen, J.F., Gao, H., Zou, H.K., Chu, G.W., Zhang, L., Shao, L., Xiang, Y., Wu, Y.X., 2010. Cationic Polymerization in Rotating Packed Bed Reactor: Experimental and Modeling. Aiche Journal 56, 1053-1062. http://dx.doi.org/10.1002/aic.11911.

Chen, J.F., Wang, Y.H., Guo, F., Wang, X.M., Zheng, C., 2000. Synthesis of nanoparticles with novel technology: High-gravity reactive precipitation. Industrial & Engineering Chemistry Research 39, 948-954. http://dx.doi.org/10.1021/ie990549a.

Chen, Y.H., Chang, C.Y., Su, W.L., Chen, C.C., Chiu, C.Y., Yu, Y.H., Chiang, P.C., Chiang, S.I.M., 2004. Modeling ozone contacting process in a rotating packed bed. Industrial & Engineering Chemistry Research 43, 228-236. http://dx.doi.org/10.1021/ie030545c.

Chen, Y.S., Lin, C.C., Liu, H.S., 2005. Mass transfer in a rotating packed bed with viscous newtonian and non-Newtonian fluids. Industrial & Engineering Chemistry Research 44, 1043-1051. http://dx.doi.org/10.1021/ie0499409.

Chen, Y.S., Lin, F.Y., Lin, C.C., Tai, C.Y.D., Liu, H.S., 2006. Packing characteristics for mass transfer in a rotating packed bed. Industrial & Engineering Chemistry Research 45, 6846-6853. http://dx.doi.org/10.1021/ie060399l.

Chen, Y.S., Liu, H.S., 2002. Absorption of VOCs in a rotating packed bed. Industrial & Engineering Chemistry Research 41, 1583-1588. http://dx.doi.org/10.1021/ie010752h.

Chu, G.W., Luo, Y., Shan, C.Y., Zou, H.K., Xiang, Y., Shao, L., Chen, J.F., 2014. Absorption of SO_2 with ammonia-based solution in a cocurrent rotating packed bed. Industrial & Engineering Chemistry Research 53, 15731-15737. http://dx.doi.org/10.1021/ie502519v.

Ding, H., Xie, P., Ingham, D., Ma, L., Pourkashanian, M., 2018. Flow behaviour of drop and jet modes of a laminar falling film on horizontal tubes. International Journal of Heat and Mass Transfer 124, 929-942. http://dx.doi.org/10.1016/j.ijheatmasstransfer.2018.03.111.

Guo, K., Guo, F., Feng, Y.D., Chen, J.F., Zheng, C., Gardner, N.C., 2000. Synchronous visual and RTD study on liquid flow in rotating packed-bed contactor. Chemical Engineering Science 55, 1699-1706. http://dx.doi.org/10.1016/S0009-2509(99)00369-3.

Guo, K., Wen, J.W., Zhao, Y., Wang, Y., Zhang, Z.Z., Li, Z.X., Qian, Z., 2014. Optimal Packing of a Rotating Packed Bed for H_2S Removal. Environmental Science & Technology 48, 6844-6849. http://dx.doi.org/10.1021/es404913e.

Guo, T.Y., Cheng, K.P., Wen, L.X., Andersson, R., Chen, J.F., 2017. Three-Dimensional Simulation on Liquid Flow in a Rotating Packed Bed Reactor. Industrial & Engineering Chemistry Research 56, 8169-8179. http://dx.doi.org/10.1021/acs.iecr.7b01759.

Guo, T.Y., Shi, X., Chu, G.W., Xiang, Y., Wen, L.X., Chen, J.F., 2016. Computational Fluid Dynamics Analysis of the Micromixing Efficiency in a Rotating-Packed-Bed Reactor. Industrial & Engineering Chemistry Research 55, 4856-4866. http://dx.doi.org/10.1021/acs.iecr.6b00213.

Hirt, C.W., Nichols, B.D., 1981. Volume of Fluid (Vof) Method for the Dynamics of Free Boundaries. Journal of Computational Physics 39, 201-225. http://dx.doi.org/10.1016/0021-9991(81)90145-5.
Hu, J.G., Yang, X.G., Yu, J.G., Dai, G.C., 2014. Numerical simulation of carbon dioxide (CO2) absorption and interfacial mass transfer across vertically wavy falling film. Chemical Engineering Science 116, 243-253. http://dx.doi.org/10.1016/j.ces.2014.05.002.
Jassim, M.S., 2002. Process Intensification: Absorption and Desorption of Carbon Dioxide from Monoethanolamine Solutions Using Higee Technology. PhD Thesis Newcastle University.
Jassim, M.S., Rochelle, G., Eimer, D., Ramshaw, C., 2007. Carbon dioxide absorption and desorption in aqueous monoethanolamine solutions in a rotating packed bed. Industrial & Engineering Chemistry Research 46, 2823-2833. http://dx.doi.org/10.1021/ie051104r.
Joel, A.S., Wang, M.H., Ramshaw, C., 2015. Modelling and simulation of intensified absorber for post-combustion CO_2 capture using different mass transfer correlations. Applied Thermal Engineering 74, 47-53. http://dx.doi.org/10.1016/j.applthermaleng.2014.02.064.
Joel, A.S., Wang, M.H., Ramshaw, C., Oko, E., 2014. Process analysis of intensified absorber for post-combustion CO_2 capture through modelling and simulation. International Journal of Greenhouse Gas Control 21, 91-100. http://dx.doi.org/10.1016/j.ijggc.2013.12.005.
Joel, A.S., Wang, M.H., Ramshaw, C., Oko, E., 2017. Modelling, simulation and analysis of intensified regenerator for solvent based carbon capture using rotating packed bed technology. Applied Energy 203, 11-25. http://dx.doi.org/10.1016/j.apenergy.2017.05.157.
Kang, J.L., Sun, K., Wong, D.S.H., Jang, S.S., Tan, C.S., 2014. Modeling studies on absorption of CO2 by monoethanolamine in rotating packed bed. International Journal of Greenhouse Gas Control 25, 141-150. http://dx.doi.org/10.1016/j.ijggc.2014.04.011.
Li, Q.S., Wang, T., Dai, C.N., Lei, Z.G., 2016. Hydrodynamics of novel structured packings: An experimental and multi-scale CFD study. Chemical Engineering Science 143, 23-35. http://dx.doi.org/10.1016/j.ces.2015.12.014.
Lin, C.C., Chen, Y.S., Liu, H.S., 2000. Prediction of liquid holdup in countercurrent-flow rotating packed bed. Chemical Engineering Research & Design 78, 397-403. http://dx.doi.org/10.1205/026387600527293.
Liu, B., Wen, Y., Liu, C., Sun, B., Yuan, X., 2016. Multiscale Calculation on Perforated Sheet Structured Packing To Predict the Liquid Distribution Based on Computational Fluid Dynamics Simulation. Industrial & Engineering Chemistry Research 55, 7810-7818. http://dx.doi.org/10.1021/acs.iecr.5b05003.
Liu, Y., Luo, Y., Chu, G.W., Luo, J.Z., Arowo, M., Chen, J.F., 2017. 3D numerical simulation of a rotating packed bed with structured stainless steel wire mesh packing. Chemical Engineering Science 170, 365-377. http://dx.doi.org/10.1016/j.ces.2017.01.033.
Llerena-Chavez, H., Larachi, F., 2009. Analysis of flow in rotating packed beds via CFD simulations-Dry pressure drop and gas flow maldistribution. Chemical Engineering Science 64, 2113-2126. http://dx.doi.org/10.1016/j.ces.2009.01.019.
Lopes, R.J.G., Quinta-Ferreira, R.M., 2009. Volume-of-Fluid-Based Model for Multiphase Flow in High-Pressure Trickle-Bed Reactor: Optimization of Numerical Parameters. AIChE Journal 55, 2920-2933. http://dx.doi.org/10.1002/aic.11862.
Lu, X., Xie, P., Ingham, D.B., Ma, L., Pourkashanian, M., 2018. A porous media model for CFD simulations of gas-liquid two-phase flow in rotating packed beds. Chemical Engineering Science 189, 123-134. http://dx.doi.org/10.1016/j.ces.2018.04.074.
Luo, Y., Chu, G.W., Zou, H.K., Zhao, Z.Q., Dudukovic, M.P., Chen, J.F., 2012. Gas-Liquid Effective Interfacial Area in a Rotating Packed Bed. Industrial & Engineering Chemistry Research 51, 16320-16325. http://dx.doi.org/10.1021/ie302531j.
Luo, Y., Luo, J.Z., Chu, G.W., Zhao, Z.Q., Arowo, M., Chen, J.F., 2017. Investigation of effective interfacial area in a rotating packed bed with structured stainless steel wire mesh packing. Chemical Engineering Science 170, 347-354. http://dx.doi.org/10.1016/j.ces.2016.10.023.
Menter, F.R., 1994. Two-equation eddy-viscosity turbulence models for engineering applications. AIAA journal 32, 1598-1605. http://dx.doi.org/10.2514/3.12149.
Nijemeisland, M., Dixon, A.G., 2001. Comparison of CFD simulations to experiment for convective heat transfer in a gas-solid fixed bed. Chemical Engineering Journal 82, 231-246. http://dx.doi.org/10.1016/S1385-8947(00)00360-0.
Ouyang, Y., Zou, H.-K., Gao, X.-Y., Chu, G.-W., Xiang, Y., Chen, J.-F., 2018. Computational fluid dynamics modeling of viscous liquid flow characteristics and end effect in rotating packed bed. Chemical Engineering and Processing: Process Intensification 123, 185-194. http://dx.doi.org/10.1016/j.cep.2017.09.005.
Ozkan, F., Wenka, A., Hansjosten, E., Pfeifer, P., Kraushaar-Czarnetzki, B., 2016. Numerical investigation of interfacial mass transfer in two phase flows using the VOF method. Engineering Applications of Computational Fluid Mechanics 10, 100-110. http://dx.doi.org/10.1080/19942060.2015.1061555.

Qi, W.Z., Guo, K., Ding, H.D., Li, D., Liu, C.J., 2017. Model prediction and optimization of dry pressure drop within Winpak. Chemical Engineering and Processing 118, 62-70. http://dx.doi.org/10.1016/j.cep.2017.04.020.
Rajan, S., Kumar, M., Ansari, M.J., Rao, D.P., Kaistha, N., 2011. Limiting Gas Liquid Flows and Mass Transfer in a Novel Rotating Packed Bed (HiGee). Industrial & Engineering Chemistry Research 50, 986-997. http://dx.doi.org/10.1021/ie100899r.
Ramshaw, C., Mallinson, R.H., 1981. Mass transfer process, US Patent No. 4283255.
Raynal, L., Royon-Lebeaud, A., 2007. A multi-scale approach for CFD calculations of gas-liquid flow within large size column equipped with structured packing. Chemical Engineering Science 62, 7196-7204. http://dx.doi.org/10.1016/j.ces.2007.08.010.
Sang, L., Luo, Y., Chu, G.W., Zhang, J.P., Xiang, Y., Chen, J.F., 2017. Liquid flow pattern transition, droplet diameter and size distribution in the cavity zone of a rotating packed bed: A visual study. Chemical Engineering Science 158, 429-438. http://dx.doi.org/10.1016/j.ces.2016.10.044.
Sebastia-Saez, D., Gu, S., Ramaioli, M., 2018. Effect of the contact angle on the morphology, residence time distribution and mass transfer into liquid rivulets: A CFD study. Chemical Engineering Science 176, 356-366. http://dx.doi.org/10.1016/j.ces.2017.09.046.
Sebastia-Saez, D., Gu, S., Ranganathan, P., Papadikis, K., 2015a. Meso-scale CFD study of the pressure drop, liquid hold-up, interfacial area and mass transfer in structured packing materials. International Journal of Greenhouse Gas Control 42, 388-399. http://dx.doi.org/10.1016/j.ijggc.2015.08.016.
Sebastia-Saez, D., Gu, S., Ranganathan, P., Papadikis, K., 2015b. Micro-scale CFD modeling of reactive mass transfer in falling liquid films within structured packing materials. International Journal of Greenhouse Gas Control 33, 40-50. http://dx.doi.org/10.1016/j.ijggc.2014.11.019.
Shi, X., Xiang, Y., Wen, L.X., Chen, J.F., 2013. CFD analysis of liquid phase flow in a rotating packed bed reactor. Chemical Engineering Journal 228, 1040-1049. http://dx.doi.org/10.1016/j.cej.2013.05.081.
Singh, R.K., Galvin, J.E., Sun, X., 2016. Three-dimensional simulation of rivulet and film flows over an inclined plate: Effects of solvent properties and contact angle. Chemical Engineering Science 142, 244-257. http://dx.doi.org/10.1016/j.ces.2015.11.029.
Singh, R.K., Galvin, J.E., Sun, X., 2017. Hydrodynamics of the rivulet flow over corrugated sheet used in structured packings. International Journal of Greenhouse Gas Control 64, 87-98. http://dx.doi.org/10.1016/j.ijggc.2017.07.005.
Singh, R.K., Galvin, J.E., Sun, X., 2018. Multiphase flow studies for microscale hydrodynamics in the structured packed column. Chemical Engineering Journal 353, 949-963. http://dx.doi.org/10.1016/j.cej.2018.07.067.
Smith, D., Graciano, C., Martinez, G., 2009. Recent Patents on Expanded Metal. Recent Patents on Materials Science 2, 209-225. http://dx.doi.org/10.2174/1874465610902030209.
Sun, B., He, L., Liu, B.T., Gu, F., Liu, C.J., 2013. A new multi-scale model based on CFD and macroscopic calculation for corrugated structured packing column. AIChE Journal 59, 3119-3130. http://dx.doi.org/10.1002/aic.14082.
Thiels, M., Wong, D.S.H., Yu, C.H., Kang, J.L., Jang, S.S., Tan, C.S., 2016. Modelling and Design of Carbon Dioxide Absorption in Rotating Packed Bed and Packed Column. Ifac Papersonline 49, 895-900. http://dx.doi.org/10.1016/j.ifacol.2016.07.303.
Uchiyama, K., Migita, H., Ohmura, R., Mori, Y.H., 2003. Gas absorption into "string-of-beads" liquid flow with chemical reaction: application to carbon dioxide separation. International Journal of Heat and Mass Transfer 46, 457-468. http://dx.doi.org/10.1016/S0017-9310(02)00301-0.
Wang, H., 1999. Partial least-squares regression-method and applications. National Defence Industry Press, Beijing.
Wang, M., Joel, A.S., Ramshaw, C., Eimer, D., Musa, N.M., 2015. Process intensification for post-combustion CO_2 capture with chemical absorption: A critical review. Applied Energy 158, 275-291. http://dx.doi.org/10.1016/j.apenergy.2015.08.083.
Wu, W., Luo, Y., Chu, G.-W., Liu, Y., Zou, H.-K., Chen, J.-F., 2018. Gas Flow in a Multiliquid-Inlet Rotating Packed Bed: Three-Dimensional Numerical Simulation and Internal Optimization. Industrial & Engineering Chemistry Research 57, 2031-2040. http://dx.doi.org/10.1021/acs.iecr.7b04901.
Xie, P., Lu, X., Ingham, D., Ma, L., Pourkashanian, M., 2017a. Mass transfer characteristics of the liquid film flow in a rotating packed bed for CO2 capture: A micro-scale CFD analysis. Energy Procedia 142, 3407-3414. http://dx.doi.org/10.1016/j.egypro.2017.12.478.
Xie, P., Lu, X., Yang, X., Ingham, D., Ma, L., Pourkashanian, M., 2017b. Characteristics of liquid flow in a rotating packed bed for CO_2 capture: A CFD analysis. Chemical Engineering Science 172, 216-229. http://dx.doi.org/10.1016/j.ces.2017.06.040.
Xing, T., Stern, F., 2010. Factors of Safety for Richardson Extrapolation. Journal of Fluids Engineering-Transactions of the Asme 132. http://dx.doi.org/10.1115/1.4001771.

Xing, T., Stern, F., 2011. Closure to "Discussion of 'Factors of Safety for Richardson Extrapolation'" (2011, ASME J. Fluids Eng., 133, p. 115501). Journal of Fluids Engineering-Transactions of the Asme 133. http://dx.doi.org/10.1115/1.4005030.

Xu, Y.Y., Paschke, S., Repke, J.U., Yuan, J.Q., Wozny, G., 2009. Computational Approach to Characterize the Mass Transfer between the Counter-Current Gas-Liquid Flow. Chemical Engineering & Technology 32, 1227-1235. http://dx.doi.org/10.1002/ceat.200900099.

Xu, Y.Y., Zhao, M., Paschke, S., Wozny, G., 2014a. Detailed Investigations of the Countercurrent Multiphase (Gas-Liquid and Gas-Liquid-Liquid) Flow Behavior by Three-Dimensional Computational Fluid Dynamics Simulations. Industrial & Engineering Chemistry Research 53, 7797-7809. http://dx.doi.org/10.1021/ie500047a.

Xu, Z., Sun, W.Q., Lu, Y., Mao, Y.H., Xie, Y.C., 2014b. Experimental Study of Falling-film Mode Transitions between Horizontal Tubes in CaCl2/Water Absorber. Journal of Thermal Science 23, 338-345. http://dx.doi.org/10.1007/s11630-014-0715-5.

Yan, Z.Y., Lin, C., Ruan, Q., 2012. Hydrodynamics in a Rotating Packed Bed. I. A Novel Experimental Method. Industrial & Engineering Chemistry Research 51, 10472-10481. http://dx.doi.org/10.1021/ie202257t.

Yan, Z.Y., Lin, C., Ruan, Q., 2014. Dynamics of droplets and mass transfer in a rotating packed bed. AIChE Journal 60, 2705-2723. http://dx.doi.org/10.1002/aic.14449.

Yang, K., Chu, G.W., Zou, H.K., Chen, J.F., 2011. Visualization of micro-fluid flow in a rotating packed bed using particle image velocimetry method. Journal of Beijing University of Chemical Technology (Natural Science Edition) 38, 7-11.

Yang, X., Ingham, D., Ma, L., Srinivasan, N., Pourkashanian, M., 2017. Ash deposition propensity of coals/blends combustion in boilers: a modeling analysis based on multi-slagging routes. Proceedings of the Combustion Institute 36, 3341-3350. http://dx.doi.org/10.1016/j.proci.2016.06.060.

Yang, Y.-C., Ouyang, Y., Zhang, N., Yu, Q.-J., Arowo, M., 2018. A review on computational fluid dynamic simulation for rotating packed beds. Journal of Chemical Technology & Biotechnology. http://dx.doi.org/10.1002/jctb.5880.

Yang, Y., Xiang, Y., Chu, G., Zou, H., Sun, B., Arowo, M., Chen, J.-F., 2016. CFD modeling of gas–liquid mass transfer process in a rotating packed bed. Chemical Engineering Journal 294, 111-121. http://dx.doi.org/10.1016/j.cej.2016.02.054.

Yang, Y.C., Xiang, Y., Chu, G.W., Zou, H.K., Luo, Y., Arowo, M., Chen, J.F., 2015a. A noninvasive X-ray technique for determination of liquid holdup in a rotating packed bed. Chemical Engineering Science 138, 244-255. http://dx.doi.org/10.1016/j.ces.2015.07.044.

Yang, Y.C., Xiang, Y., Li, Y.G., Chu, G.W., Zou, H.K., Arowo, M., Chen, J.F., 2015b. 3D CFD modelling and optimization of single-phase flow in rotating packed beds. Canadian Journal of Chemical Engineering 93, 1138-1148. http://dx.doi.org/10.1002/cjce.22183.

Youngs, D.L., 1982. Time-dependent multi-material flow with large fluid distortion. Academic Press, New York.

Yu, C.-H., Chen, M.-T., Chen, H., Tan, C.-S., 2016. Effects of process configurations for combination of rotating packed bed and packed bed on CO2 capture. Applied Energy 175, 269-276. http://dx.doi.org/10.1016/j.apenergy.2016.05.044.

Zhang, J., Guo, K., Guo, F., Zhu, J., Zheng, C., 2000. Experimental Study about Flow of Liquid in Rotating Packed Bed. Journal of Chemical Engineering of Chinese University 14, 378-381.

Zhang, J.P., Luo, Y., Chu, G.W., Sang, L., Liu, Y., Zhang, L.L., Chen, J.F., 2017. A hydrophobic wire mesh for better liquid dispersion in air. Chemical Engineering Science 170, 204-212. http://dx.doi.org/10.1016/j.ces.2017.03.058.

Zhao, B.T., Su, Y.X., Tao, W.W., 2014. Mass transfer performance of CO2 capture in rotating packed bed: Dimensionless modeling and intelligent prediction. Applied Energy 136, 132-142. http://dx.doi.org/10.1016/j.apenergy.2014.08.108.

Zheng, X.H., Chu, G.W., Kong, D.J., Luo, Y., Zhang, J.P., Zou, H.K., Zhang, L.L., Chen, J.F., 2016. Mass transfer intensification in a rotating packed bed with surface-modified nickel foam packing. Chemical Engineering Journal 285, 236-242. http://dx.doi.org/10.1016/j.cej.2015.09.083.

Zou, H.K., Sheng, M.P., Sun, X.F., Ding, Z.H., Arowo, M., Luo, Y., Zhang, L.L., Chu, G.W., Chen, J.F., Sun, B.C., 2017. Removal of hydrogen sulfide from coke oven gas by catalytic oxidative absorption in a rotating packed bed. Fuel 204, 47-53. http://dx.doi.org/10.1016/j.fuel.2017.05.017.

Highlights

- A new mesoscale 3D CFD model is proposed to predict the liquid flow in an RPB.
- Detailed liquid flow patterns in the RPB are obtained.
- Liquid holdup, percentage of droplets and interfacial area in the RPB are analysed.
- New correlations for liquid holdup and effective interfacial area are developed.
- Parametric sensitivity analyses of the RPB for influencing CO_2 capture are performed.

Declaration of interests

☒ The authors declare that they have no known competing financial interests or personal relationships that could have appeared to influence the work reported in this paper.

☐The authors declare the following financial interests/personal relationships which may be considered as potential competing interests: